LAWRENCE
LIVERMORE
NATIONAL
LABORATORY

UCRL-TR-220224

FY2005 Progress Summary and FY2006 Program Plan Statement of Work and Deliverables for Development of High Average Power Diode-Pumped Solid State Lasers, and Complementary Technologies, for Applications in Energy and Defense

C. Ebbers

March 29, 2006

Disclaimer

This document was prepared as an account of work sponsored by an agency of the United States Government. Neither the United States Government nor the University of California nor any of their employees, makes any warranty, express or implied, or assumes any legal liability or responsibility for the accuracy, completeness, or usefulness of any information, apparatus, product, or process disclosed, or represents that its use would not infringe privately owned rights. Reference herein to any specific commercial product, process, or service by trade name, trademark, manufacturer, or otherwise, does not necessarily constitute or imply its endorsement, recommendation, or favoring by the United States Government or the University of California. The views and opinions of authors expressed herein do not necessarily state or reflect those of the United States Government or the University of California, and shall not be used for advertising or product endorsement purposes.

This work was performed under the auspices of the U.S. Department of Energy by University of California, Lawrence Livermore National Laboratory under Contract W-7405-Eng-48.

FY2005 Progress Summary
and FY2006 Program Plan
Statement of Work and Deliverables

For

Development of High Average Power Diode-Pumped Solid State Lasers, and Complementary Technologies, for Applications in Energy and Defense

Prepared by Dr. Chris Ebbers
Mercury Laser Project Scientist
Lawrence Livermore National Laboratory
(925) 423-9465

Presented to
Dr. Tom Finn, DP/DOE,
Virtual Office of Inertial Fusion Energy

Continuation of DOE Contract Number DE-AI03-94SF19892

Document release 1.2

For further information contact:

Dr. Wayne Meier
Deputy Program Leader for IFE
Phone: (925) 422-8536
meier5@llnl.gov
or
Dr. Camille Bibeau
Project Leader for Mercury Laser
Phone: (925) 422-7798
bibeau1@llnl.gov

Lawrence Livermore National Laboratory
Livermore, CA 94550

TABLE OF CONTENTS

FY2005 PROGRESS SUMMARY

TABLE OF CONTENTS

1.0 DPSSL Development

1.0.1 Executive Summary

The primary focus this year was to operate the system with two amplifiers populated with and pumped by eight high power diode arrays. The system was operated for extended run periods which enabled average power testing of components, diagnostics, and controls. These tests were highly successful, with a demonstrated energy level of over 55 joules for 4 cumulative hours at a repetition rate of 10 Hz (average power 0.55 kW). In addition, high average power second harmonic generation was demonstrated, achieving 227 W of 523.5 nm light (22.7 J, 10 Hz, 15 ns, 30 minutes) Plans to achieve higher energy levels and average powers are in progress.

The dual amplifier system utilizes a 4-pass optical arrangement. The Yb:S-FAP slabs were mounted in aerodynamic aluminum vane structures to allow turbulent helium gas flow across the faces. Diagnostic packages that monitored beam performance were deployed during operation. The laser experiments involved injecting a seed beam from the front end into the system and making four passes through both amplifiers. Beam performance diagnostics monitored the beam on each pass to assess system parameters such as gain and nearfield intensity profiles. This year, an active mirror and wavefront sensor were procured and demonstrated in an off-line facility. The active mirror technology can correct for low order phase distortions at user specified operating conditions (such as repetition rates different than 10 Hz) and is a complementary technology to the static phase plates used in the system for higher order distortions.

A picture of the laser system with amplifier #2 (foreground) and amplifier #1 (background) is shown in Fig. 1.0.1.1. The control system and diagnostics were recently enhanced for faster processing and allow remote operation of the system.

Figure 1.0.1.1 Photograph of the two amplifier Mercury laser laboratory

The growth and fabrication of the Yb:S-FAP slabs constituted another major element of our program objectives. Our goal was to produce at least fourteen 4x6 cm^2 crystalline slabs. These goals were met. Nine crystal boules were successfully grown to produce 14 slabs. In addition, we have prepared the way to scale the Yb:S-FAP crystals to the next growth diameter (10" diameter as opposed to 7" diameter). An outside contract was placed with Northrop-Grumman to scaleup the Yb:S-FAP crystal size. The following sections discuss the above accomplishments in more technical detail and are followed by plans and a budget request for FY2006.

1.1 Fabricate Yb:S-FAP Crystals

Continue fabrication and growth of gain media for mercury laser both at LLNL and commercial facilities. Produce coated and characterized slabs for the laser system.

The goals of the high temperature crystal growth effort were to produce high quality Yb:S-FAP [Yb^{3+}:$Sr_5(PO_4)_3F$] crystalline slabs. Each of the two amplifier assemblies requires seven slabs of dimension 4 x 6 x 0.75 cm (Fig. 1.1.1). In this fiscal year, 7.0 cm diameter boules were produced at Northrop-Grumman that are each capable of yielding 2 full size amplifier slabs. The LLNL facility was upgraded to 7.0 cm diameter capability from the previous 3.5 cm diameter growth to allow yields of up to two full size slabs from each boule. The objective of the growth effort at Northrop-Grumman was to produce slabs for the Mercury laser and improve the optical quality and yield while ultimately developing a commercial source for Yb:S-FAP crystals. Nine boules were grown yielding 8 full size slabs with 6 additional slabs expected upon further fabrication.

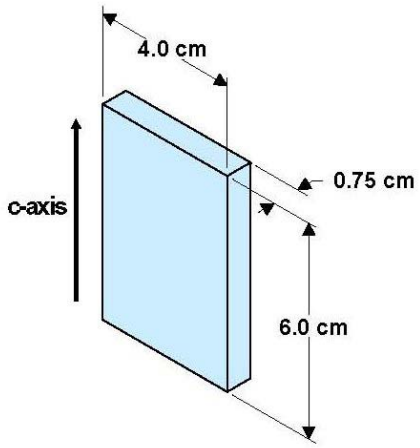

Figure 1.1.1 Schematic of the Yb:S-FAP slab dimensions required for the Mercury design.

1.1.1 Czochralski Crystal Growth

Crystals of Yb:S-FAP are grown by using the Czochralski method in three growth stations at LLNL and one growth station at Northrop-Grumman. The LLNL facility has been upgraded with three larger growth stations and power supplies to provide 7.0 cm diameter growth capability. Northrop-Grumman has continued to grow 7.0 cm diameter crystals and improve the optical quality. The growth is initiated from a 7 x 7 mm seed at a temperature of 1786 °C in a standard oxide-type Czochralski furnace design. Growth involves a seed extension, ramping the diameter out to 7.0 cm and stable growth at 7.0 cm for up to a 10 cm length at 0.5 mm/hr pull rate and 15 rpm rotation rate. Chillers, a motor generator and new, regulated power supplies have been employed to stabilize fluctuations to the growth and increase reliability. Each boule takes approximately 24 days to complete and has a potential yield of two full size slabs. Figure 1.1.2 shows the 9 boules produced in FY2005.

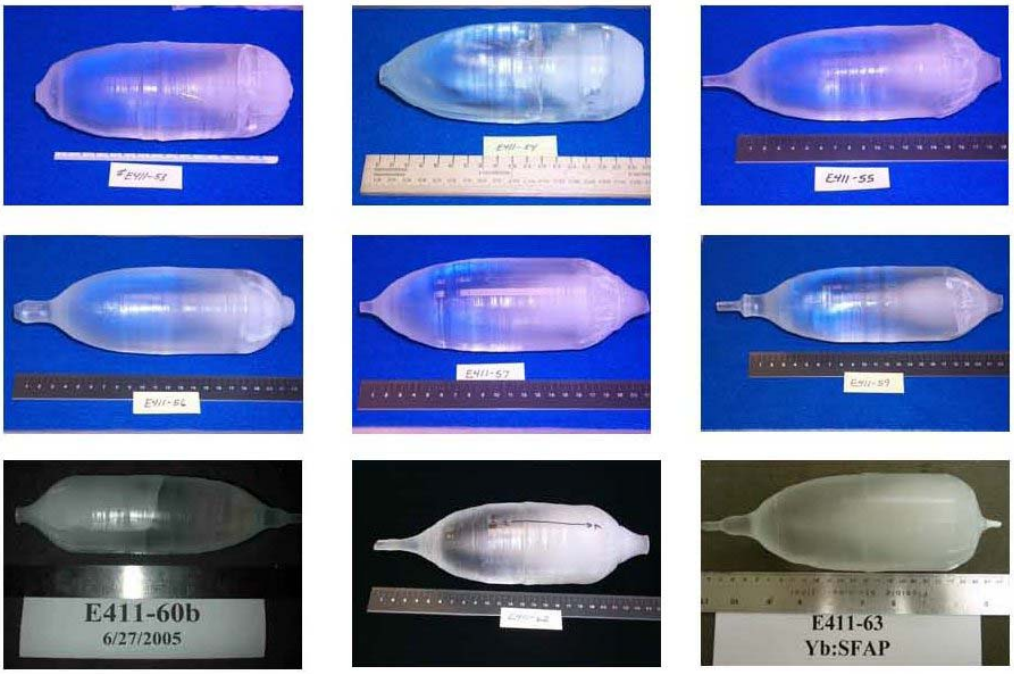

Figure 1.1.2 Picture of 7.0 cm diameter Yb:S-FAP boules grown in FY2005.

The boules in Figure 1.1.2 yielded 14 slabs that were fabricated for the Mercury Laser. As the size of the boules increase, the grain boundaries must be properly managed. In the past year, grain boundaries have been significantly reduced by approximately 60%. This was accomplished by controlling the cooling of the boule during growth by altering temperature gradients within the furnace. The Northrop-Grumman furnace was modified to allow nitrogen to flow through from the bottom-to-the-top, past the crucible and growing boule. By changing the flow rate of the nitrogen, the cooling of the boule is better controlled and stress within the boule is minimized. The nitrogen reduces the formation of grain boundaries since they are formed as a result of dislocations that migrate together to relieve stress in the boule upon cooling. Experiments are in progress to further reduce grain boundaries and increase the optical quality of the slabs.

Once the crystal is grown there are several fabrication steps required to create a full sized slab. The boule first undergoes cutting and polishing to determine the suitability to produce slabs. Then the crystals are fabricated for water jet cutting with a thin, high-pressure stream of water that does not induce heating during the cut that might result in cracking. Each cut boule is then shaped into full size slabs.

The final polishing steps have been successfully transferred to a commercial vendor where a conventional polish is placed on one side of the slab and Magneto-rheological finishing (MRF) is used on the second side to remove subsurface damage and to yield flat transmitted wavefronts with less than 1 nm of surface roughness. We have worked with the vendor to improve the quality of the conventional polished surface to greatly limit the number of sleeks and defects that could be a source of optical damage. This involved modifying the polishing slurry and changing the pre-polished, rough surface to be slightly concave. MRF varies from

conventional polishing techniques by polishing via a magnetic slurry that is forced over the surface of the Yb:S-FAP slab in a sheering motion by a magnetic ribbon. This is a well known technique for removing imperfections in the transmitted wavefront of optics by imprinting the reverse wavefront on the surface of the slab. MRF has been invaluable in reducing wavefront errors and to improving the transmitted wavefront. Currently, thirteen slabs have been corrected for transmitted wavefront by MRF in FY2005 and four additional slabs are awaiting MRF.

In this year, we have increased our efforts to measure the damage limits of Yb:S-FAP slabs and the mechanisms that contribute to damage. The current fluence limitations have been measured at a commercial vendor and results for various. It has been found that an MRF polish on Yb:S-FAP can endure fluences up to ~13 J/cm^2 at 10 ns, compared to conventional polished surface ($\geq$ 22 J/cm^2). As expected, uncoated surfaces can survive up to fluences $\geq$ 50 J/cm^2. In addition, initiation of damage is quite different than growth of damage. Initial tests have indicated that no growth of damage will occur until 30 J/cm^2. This means that even though small damage sites may be initially created, these sites will not grow unless exposed to substantially higher fluences. Further testing of initiation and growth are ongoing as material improvements are made.

We are continuing to work with a commercial vendor to explore a low-temperature solution-based bonding technique for Yb:S-FAP. Bonding allows larger slabs to be formed form smaller high quality parts. The low temperature method offers the possibility of a stronger bond and a simpler process. The technique is currently being modified from an existing technique that is used for bonding silicate and phosphate-based glasses where a chemical solution is placed between two polished crystals and reacts with the surface to form strong bonds while evaporating away any liquid that is a by-product. Initial experiments have been encouraging on small samples, however, the chemistry of Yb:S-FAP crystals is sufficiently different from the glasses previously bonded by this method, that more chemistry research is required to a develop compatible solution. Currently, we are testing the flatness requirements of the surfaces, modifying the bonding solution, and preparing the crystal surface to readily accept and bond with the solution. Analytical methods are being employed to refine the process and guide choices.

We are working with Northrop-Grumman to begin the growth of $\geq$ 10 cm diameter Czochralski growth of Yb:S-FAP for laser systems beyond the Mercury Laser. The growth station and furnace have been built and are ready for the initial experiments that will take place in the early part of FY2006.

In summary, 7.0 cm diameter Yb:S-FAP boules are being reproducibly grown at Northrop-Grumman. Two of three growth stations at LLNL have been upgraded to 7.0 cm diameter growth, with a third coming online in early FY2006. In FY2005, 9 boules were grown, yielding 8 full size slabs for the Mercury Laser, with 6 additional slabs expected upon further fabrication. Grain boundaries have been reduced by 60% in these slabs and the yield of slabs per boule has significantly increased. In the upcoming year, a feasibility study for larger (>10 cm diameter) crystals will be completed.

1.2 Full System Activation with Two Yb:S-FAP Amplifiers

Activate system with two gas cooled amplifiers and wavefront correction for average powers of >250 W at 1.047 mm. Diagnose performance with a suite of diagnostic packages to measure spatial, temporal, and energy characteristics. Benchmark codes with data.

1.2.1 Architecture

The Mercury architecture utilizes a diode end-pumped scheme in which the diode light and laser light are co-propagating. Each amplifier assembly is pumped by two set of 100 kW diode arrays to provide 12.3 nepers of total gain for 100 J of desired output. The diode light is first angularly redistributed by hollow concentrating optics to a 3x5 cm aperture to provide homogeneous angular divergence in both the horizontal and vertical directions. The diode light is then guided by a rectangular reflective cavity called a 'homogenizer', which maintains the angular distribution while spatially smoothing the diode pump profile. The 1047 nm extraction beamline employs an off-axis, four-pass configuration whereby each pass utilizes pinholes tailored in size to optimally filter noise on the beam while accommodating high power. The beam is propagated at 8 mrad relative to the optic axis allowing 2.8 cm beam separation near focus. Passive 4-pass amplification eliminates the need for a high average power output optical switch. To reduce buildup of parasitic beams, a thermal birefringence-compensated Pockels cell is used after two passes where the average power is less than 200W. To increase reliability and minimize the beam modulation, relay imaging is employed in the optical layout.

During FY2005, the Mercury laser upgraded selected components to allow increased energy and temporal stability. The front end was modified to add pulse shaping capabilities and reduce timing jitter. The new single longitudinal mode oscillator is temporally chopped by an acousto-optic Q-switch and injected by a fiber optic into an arbitrary waveform generator (AWG). The AWG utilizes an integrated lithium niobate modulator to shape the pulse via 96 independent temporal channels which are 250 picoseconds long. The AWG allows modification of the shape and length of the pulse and to pre-correct for square pulse distortion (an effect of temporal gain saturation) on the output pulse. The shaped pulse is then injected into a 3-meter regenerative amplifier which amplifies the 3-15 ns long pulses from the nanojoule level up to the 10 mJ level. The output of the regenerative amplifier is then double passed through two 9 mm Nd:YLF amplifier rods to produce up to 500 mJ of output energy in a shaped pulse at 10 Hz. Even though only 10-50 mJ are needed for injection into the laser, the front end is run in a saturated mode to flatten the spatial mode and increase energy stability.

The fluence on the optics in the reverser was reduced to allow more operating margin (Figure 1.2.1.1). The reverser optics were moved further from focus in order to distribute the energy over a larger area of the mirror. By increasing the multiplexing angle from 5 mrad to 8 mrad, the beams are separated from focus. A more subtle change that also effected beam separation was the clocking angle of the beams at focus. The clocking positions were changed from a cross pattern to a rectangular pattern. In addition, a new motorized pinhole manipulators were fabricated which allow motorized insertion, independent sizing, and positioning of each pinhole for optimal efficiency or beam quality as desired. In preparation for remote operation, we have begun replacing manual micrometers on mirrors with motorized units that can be controlled by a computer. Now adjustments to the reverser optics, which previously required opening of the vacuum system, are performed without breaking vacuum through motorized

mounts. In addition, optics which need adjustment during operations such as the front end waveplate for setting the front end injection energy are also motorized.

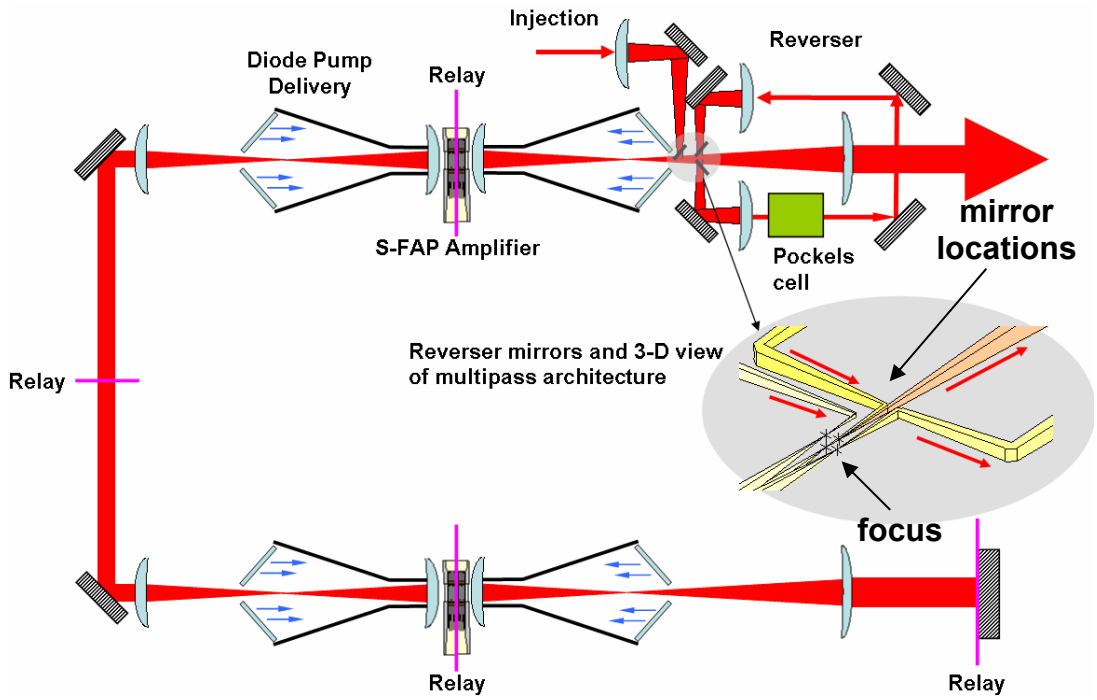

Fig. 1.2.1.1 Schematic drawing of the laser architecture with inset showing placement of reverser mirrors. Moving the mirrors further from focus decreases the fluence below the damage threshold.

The last hardware modifications allow new frequency conversion capabilities. For added accessibility and flexibility in beam size, a new optical table was installed in the Mercury lab at the output with a telescope capable of either 1:1 relay imaging or demagnification depending on the optimal intensity and thickness requirements of a particular frequency conversion module being tested (Fig. 1.2.1.2). The frequency conversion plates, are housed in an enclosure which provides user specified atmosphere (either dry nitrogen or helium), as well as water cooling, motorization, and thermocouple spigots, to respectively cool, angularly tune, and monitor the steady state temperature of the frequency converter during average power operation. Since the 1ω and 2ω output laser pulses are currently not being used for target experiments, the average power needs to be safely dumped during operations. As a result, a new method of dumping the energy was devised using low concentrations of cobalt nitrate (for absorbing 2ω) and copper nitrate (for absorbing 1ω) in chilled water. The mixture is contained in a continuously flowing cell.

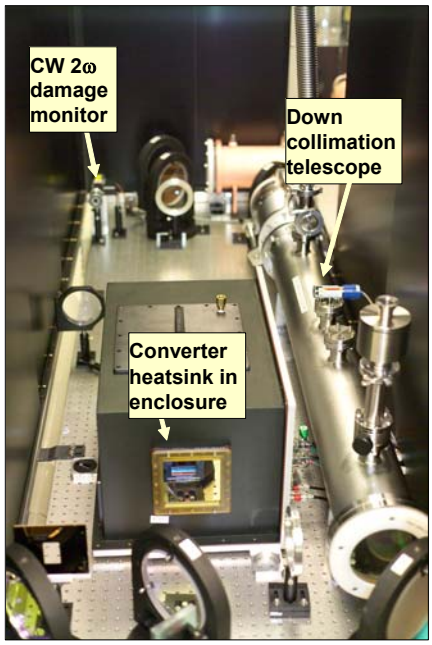

Fig. 1.2.1.2 Photo of installed hardware showing new frequency conversion capability.

1.2.2 Controls and Diagnostics

The controls and data acquisition are nearly automated for 10 Hz laser operation. A suite of diagnostics allows the beam attributes to be measured on each pass. In particular, real-time observation diagnostics and image differencing algorithms allow rapid detection of beam events at 10 Hz. When the computer software algorithm detects an obscuration > 100 μm a signal is sent to the control system to terminate operations before the next shot. The controls and diagnostics on the Mercury laser were enhanced to provide increased reliability and stability of measured signals.

Initial operation of the laser system with the Pockels cell and Bournlea pulser produced electro-magnetic frequency (EMF) spikes. The spurious noise affected the diagnostics signals and produced: false triggering of cameras and acquisition loops, noise on energy waveform effecting the measured energy stability, and temporal noise effecting the measured temporal waveform and arose from an imperfect termination at the Pockels cell. The electrical connection was upgraded to a configuration that utilizes a split charge line, along with better shielding, ferrite inductance loops, and specialty monitoring electronics. This new configuration was tested during Mercury operations without any of the adverse EMF.

In order to increase system shielding resistance to EM radiation, the cabling was upgraded from RG 223 to TMR400, providing and additional 20 dB increase in shielding. In addition, ferrite inductive loops were installed on all of the timing cabling to attenuate high frequency noise. High impedance electronics such as the energy diagnostics were connected locally to low noise amplifiers to provide 50 ohm termination before transmitting the signal to the control system.

Diagnostics that detect obscurations in the beam were improved through the addition of a continuous-wave (CW) probe laser to allow constant signal level on the cameras. A 1064 nm CW probe laser is injected collinearly with the front end pulsed beam. The CW probe is on at all

times and does not affect the extraction because there is no gain in Yb:S-FAP at 1064 nm. In the diagnostic path, a splitter samples both the CW and pulsed beams. The beam is focused onto the darkfield stop, where low spatial frequency information from the laser beam is absorbed, while the high frequency information is transmitted and imaged onto a camera. The camera is fitted with 1064 nm narrowband pass filters which reflect the pulsed 1047 nm extraction beam and pass the 1064 CW diagnostic. The advantages of this setup are that the signal levels allow constant reference images to be obtained.

Efforts were begun this year to monitor and improve beam quality of the laser. Phase aberrations are corrected in the S-FAP slabs utilizing a combination of static corrector plates as well as magneto-rheological finishing applied directly to S-FAP to reduce high order frequency aberrations from grain boundaries. An adaptive optical system was identified and ordered. Wavefront sensors were installed to monitor system static and thermal wavefront, and the laser output farfield camera was motorized along the beam propagation direction to allow M^2 or output beam quality measurement. The wavefront sensors (manufactured by Wavefront Sciences, Inc.) detect the wavefront using a Shack-Hartmann (or lenslet) array mounted in front of a CCD camera. The system includes analysis tools which provides intensity, wavefront, and gradient data for use in system models.

The diagnostics and control system is currently comprised of over 50 computers and 63 diagnostic points. A suite of post-data-collection analysis tools has been written to automatically format the acquired data including energy, temporal, nearfield, and farfield data. The Mercury server storage has been increased from a 1 terabyte (TB) system to a 4 TB system. This increase in storage capacity is driven by the anticipated data loads – during typical 1 hour, 10 Hz laser operation run up to one hundred gigabytes of data can be acquired.

1.2.3 Mercury Laser Operations

In the final fabrication step the Yb:S-FAP slabs are mounted into the aerodynamic structures we call “vanes”, which enable high speed gas-cooling and 10 Hz operation. The vanes are first lined with highly absorbing edge cladding (Schott KG5 glass) which is 300 μm thick, and then the slabs are potted into the vanes with an elastomer that provides a compliant insulating barrier to protect the slab from thermal and mechanical stresses. Seven vanes are assembled together where each vane is separated by one-millimeter wide helium gas cooling channels to form the amplifier cassette (Fig. 1.2.3.1). At 45 psi and 0.1 Mach flow, the cooling system removes 1-3 W/cm^2 from the faces of each slab. After installation of 14 amplifier slabs in the system, flow stability and thermal wavefront were measured since this represented the first set of experiments with a fully populated amplifier. The amplifier heads were each tested for flow compliance and found to have less than 0.12% rms pressure deviation between gas channels. The amplifier heads were thermally tested at 20% beyond the designed thermal load with approximately one wave of distortion per amplifier cassette. The thermal wavefront shows approximate agreement with a thermo-mechanical model of the amplifier slabs. From the temperature profile, the model is able to calculate the total phase distortion due to the effects of thermal expansion, bulk stress, and the change of refractive index with temperature.

An experimental campaign was focused on demonstrating the system at 0.5 kW. The gain was increased by holding the front end energy constant (10 mJ) and increasing the diode pulse length from 300 to 900 μsec. At each operating point the system was tested for parasitics, ASE losses, and gain. An energetics model that includes diode pumping, pump saturation, gain, amplified spontaneous emission, passive optical losses, and gain saturation is plotted in Fig.

1.2.3.2. Temporal pulse shaping is used to compensate for the square pulse distortion caused by gain saturation. The system was run at the 10 Hz design point at 55 J for a cumulative total of seven hours (Fig. 1.2.3.2c) with an rms energy fluctuation of 3% with more than 80% of the energy in a 6 times diffraction-limited spot.

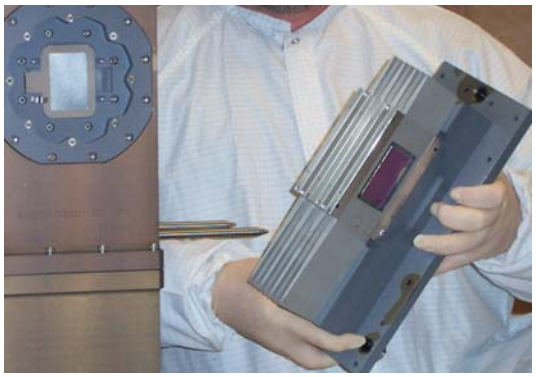

Figure 1.2.3.1 Gas-cooled amplifier cassette with vanes removed.

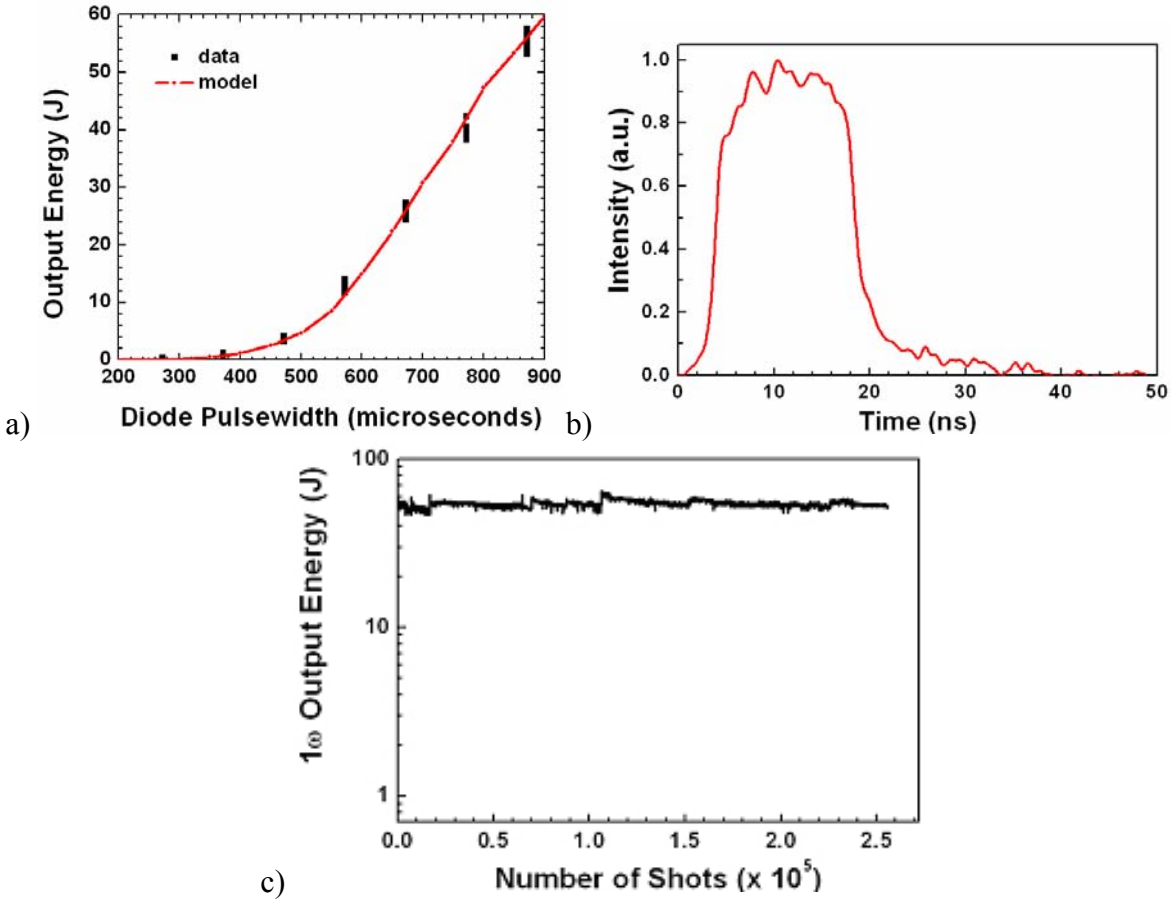

Fig. 1.2.3.2 a) Energetics gain curve showing agreement with model, b) 15 ns FWHM shaped output laser pulse, c) average power operation at 55 J for over 2.5 x 10^5 shots showing 3% rms energy fluctuation.

1.2.4. KiloJoule Class Systems Modeling

As part of our continuing effort to evaluate new ion/host combinations and laser geometries appropriate for follow on diode-pumped solid-state laser systems to the Mercury Laser, we have initiated a trade study of several potentially interesting systems. To keep the effort manageable and to ensure we could get to a point of making at least a preliminary recommendation within a 1 year time frame we adopted a solid-state point design with the following characteristics:

- 4 MJ @ 1ω
- 10 Hz PRF
- >10% wall plug efficiency
- 48 chamber ports
- ~ 1 W/cm^2 heat dissipation at laser slabs

The 4 MJ @ 1ω, the 10 Hz rep rate, and the >10% wall plug efficiency characteristics were chosen to keep continuity with the current HAPL design goals. The 48 chamber ports requirement deviated from the standard HAPL 60 port chamber design goal, but was chosen here to simplify laser-to-chamber coupling issues and to leverage design concepts on the National Ignition Facility (NIF). The final characteristic of 1 W/cm^2 of dissipated heat at the laser slabs was chosen to ensure compatibly with He cooling and to leverage cooling technology designs already validated by the Mercury laser system. Our intent at the start of this activity was to carry the study of the various competing systems at least to the point that would allow us to trade off against each other, the various strengths and weaknesses presented by the competing designs. The ultimate criteria that we adopted for discriminating between various designs were technical risk and cost of electricity. Although it was not expected that we would arrive at a definitive view of these issues in the one year time frame of this particular study, it was our intent to establish a collection of models and flow down analysis for further detailed studies..

A key component of our strategy was to leverage the knowledge and experience base of both the Mercury laser system and the NIF laser system. Table 1.2.4.1 details various NIF technologies and how those technologies would have to be upgraded to enable a 4 MJ, 10 Hz laser. Figure 1.2.4.2 illustrates high-average-power beam line components and technologies which were developed under the Mercury laser Project and were used to evaluate the follow on designs to the Mercury laser under investigation here. While some of the technologies in Table 1.2.4.1 and Fig. 1.2.4.2, such as laser diode arrays and He cooling are now well developed and have been credibly demonstrated as a direct result of the Mercury Laser project, others remain to be refined to a more convincing level, such as Yb:S-FAP crystal growth, and still others have not even begun to be evaluated or demonstrated, such as a high average power plasma emission Pockels cell (PEPC).

In the end three different laser systems using three different gain media were put forward for our investigation:

1. Yb:S-FAP based system
2. Nd:Glass based system
3. Transparent optical ceramic based system

Figure 1.2.4.3 details the gain media used in the three systems and Table 1.2.4.4 details the relative strengths and weaknesses of the various materials from the perspective of the 4 MJ, 10

Hz laser system. Two of these systems are closely traceable to either the present Mercury laser or NIF laser system, while the third represents a hybrid of the Mercury and NIF systems.

NIF technology	Beam line upgrade to enable 10 Hz operation
Flashlamps	Diode arrays
4.3 cm thick Nd:Glass slabs	• Thinner Nd:Glass slabs • Yb:YAG ceramic slabs • Mercury-like Yb:S-FAP amplifier heads
KDP PEPC (optical switch)	DKDP PEPC (optical switch)
Air slab cooling	He cooling
KDP harmonic generation	• DKDP harmonic generation • YCOB harmonic generation

Table 1.2.4.1. NIF technology upgrades required for a 10 Hz, 4 MJ laser

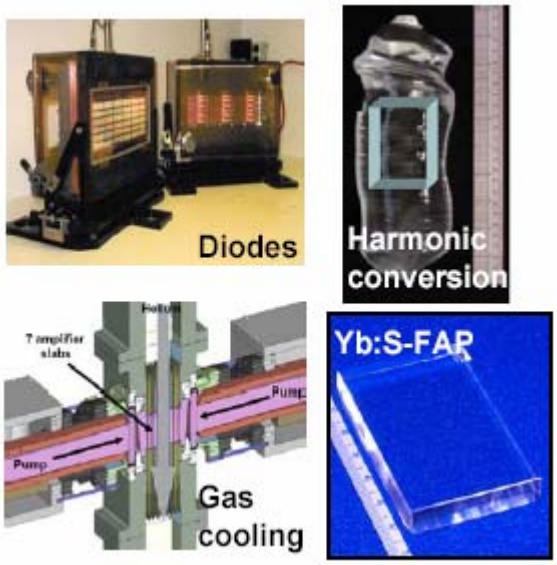

Fig. 1.2.4.2 Our modeling exercise draws heavily on high-average-power beam line components and technologies developed for the Mercury laser

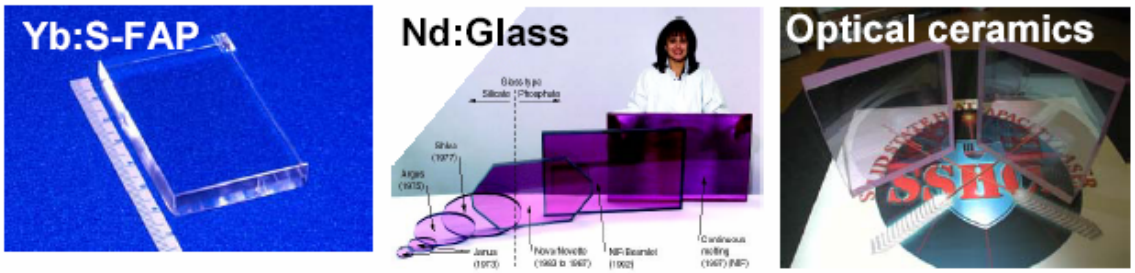

Fig. 1.2.4.3 The three different optical materials shown above: Yb:S-FAP, Nd:Glass, and optically transparent ceramic YAG were evaluated for there potential value to a 4 MJ, 10 Hz diode-pumped laser system.

Table 1.2.4.4 Relative comparison of evaluated gain media

	Yb:S-FAP	Nd:Glass	Yb:YAG transparent ceramic
Strengths	1 msec storage lifetime Ideal spectroscopy for IFE laser Thermal conductivity 2 W/m/K	Large apertures (NIF slabs are 40 x 70 cm) Established Production Four level laser	Crystalline material but scales like glass Optical quality comparable to glass Rapid development path due to many users Thermal conductivity 8 W/m/K
Weaknesses	Single developer Limited aperture Quasi-three level laser	3x lower storage lifetime than Yb^{3+} Thermal conductivity 0.6 W/m/K	Currently applicable to cubic structures – YAG, Yttria, etc.

Table 1.2.4.5 gives a side by side comparison of the three solid state laser systems highlighting diode-pump requirements and slab cooling requirements. The diode requirements of the Yb:S-FAP and Yb:YAG systems are the same at 20 GW of peak pump power, while the Nd:Glass system requires 56 GW. These diode peak power requirements are driven by a combination of the energy storage time of the ions used by the particular systems and the 20% optical-optical conversion efficiency requirement. To first order, all ions are pumped for the same number of storage lifetimes, so Nd^{3+} with its ~360 μsec storage time requires about 3x more diodes than the Yb^{3+} based systems with their 1 msec storage time. Beyond the diode pump requirements, the most striking difference in three options is the cooling requirement at the slabs, with the Yb:S-FAP and Nd:Glass system requiring less than 20 MW of consumed power to thermally manage the slabs, while the Yb:YAG system requires 111 MW. The reason for this difference is that the Yb:YAG slabs have to be held at 100 K, while the Yb:S-FAP and Nd:Glass slabs are held at room temperature. Although the forgoing combination of diode pump requirements and cooling requirements would appear to strongly favor Yb:S-FAP as the preferred option for a 4 MJ IFE laser system, there are challenges with the fabrication of the area-scaled Yb:S-FAP slabs that would be required for a 4 MJ system.

Table 1.2.4.5 Comparison of diode requirements and slab cooling for the three diode-pumped laser systems under consideration.

	Yb:S-FAP	**Nd:Glass**	**Yb:YAG (100 K)**
Laser type	Quasi-three level	Four level	Four level
Diode pump power	20 GW	56 GW	20 GW
Absorption FWHM	3.4 nm	12.5 nm	15 nm
Aperture size	13 x 20 cm (near normal incidence)	40 x 40 cm (Brewster)	40 x 40 cm (Brewster)
Beam lines	768	192	384
$P_{thermal}$ from laser slabs and operating temperature	23 MW 268 K	42 MW 268 K	16 MW 100 K
COP_{th} (Q/W)	9.4	9.4	0.17
Power required for thermal management	17.1 MW	19.1 MW	111 MW

Figure 1.2.4.6 illustrates another difference between the three systems and the conceptualized beam lines that we have analyzed for each. Because we anticipate the availability of 40 cm x 70 cm slabs in the case of the Yb:YAG ceramic, and such size glass slabs are already produced for NIF, we have adopted what is essentially a NIF beam line for each of these systems. The Yb:S-FAP with its smaller assumed slab size of 20 cm x 30 cm, and higher pump irradiance requirements than the other systems, maintains a beam line geometry driven by the present Mercury laser system with its closely spaced, and near normal incidence end-pumped slabs. The number of Nd:Glass beam lines required for the 4 $MJ_{1\omega}$ is 192, the same as the flash lamp pumped NIF, the number of ceramic Yb:YAG beam lines is 384, and the number of Yb:S-FAP beam lines is 768. This difference in the number of beam lines is driven by the larger emission cross section of the 100 K Yb^{3+} ion YAG relative to that of Nd^{3+} ion in glass and the slab size assumptions made for the Yb:S-FAP. One of the striking features of the beamlines illustrated in Fig. 1.2.4.6 is the very compact size of the Yb:YAG based one relative to the other two. This compact size is driven by the very favorable spectroscopy and thermal-mechanical properties of ceramic Yb:YAG at 100 K, permitting multiple slabs to be closely packed side-by-side and still be efficiently pumped at Brewster's angle. By taking advantage of this geometry, and not having to space the slabs out end-to-end as in the Nd:Glass case, the ceramic Yb:YAG beam line can be shortened enough to actually eliminate one of the intra laser spatial filters, which again leads to compacting of the beam lines.

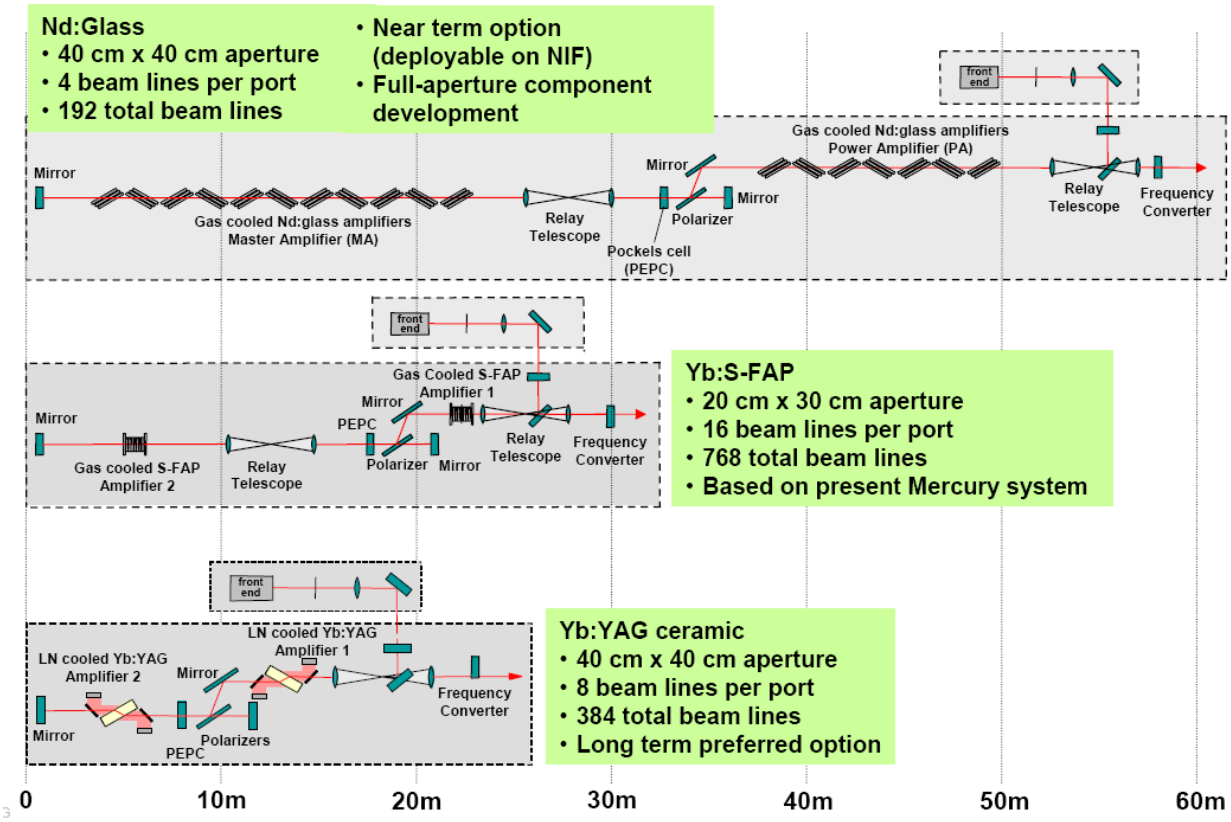

Fig. 1.2.4.6 Side by side comparison of conceptual beam lines for the three systems under investigations here. The slab sizes of the Nd:Glass and Yb:YAG systems were chosen to be 40 cm x 70 cm, while the Yb:S-FAP slab size was chosen to be 20 cm x 30 cm to mitigate the risk associated with Yb:S-FAP growth that would be required for scaled slabs.

To further optimize the Yb:YAG system performance we have analyzed laser efficiency as a function of slab temperature. Figure 1.2.4.7 illustrates the power required to manage the thermal environment of the slabs as the temperature is varied, as well as how the laser output energy varies with slab temperature. The power required to remove the heat from the slabs at cryogenic temperatures is gauged from accepted industrial scaling [1],

$$\frac{P_{\text{required for cooling}}}{P_{\text{thermal}}} = 2.5\left(\frac{T_a - T_c}{T_c}\right)^{4/3},$$

where T_a is the ambient temperature that the removed heat is dumped to, and T_c is the temperature at which the slabs are to be held. Rolling these temperature dependencies up into a single system efficiency curve, shows that optimum performance obtains at 100 K. One way to understand this is to consider the kinetics that characterize the Yb:YAG system. Above ~120 K, the Yb:YAG behaves as a quasi-three-level laser system with its performance strongly driven by ground state absorption considerations, while below

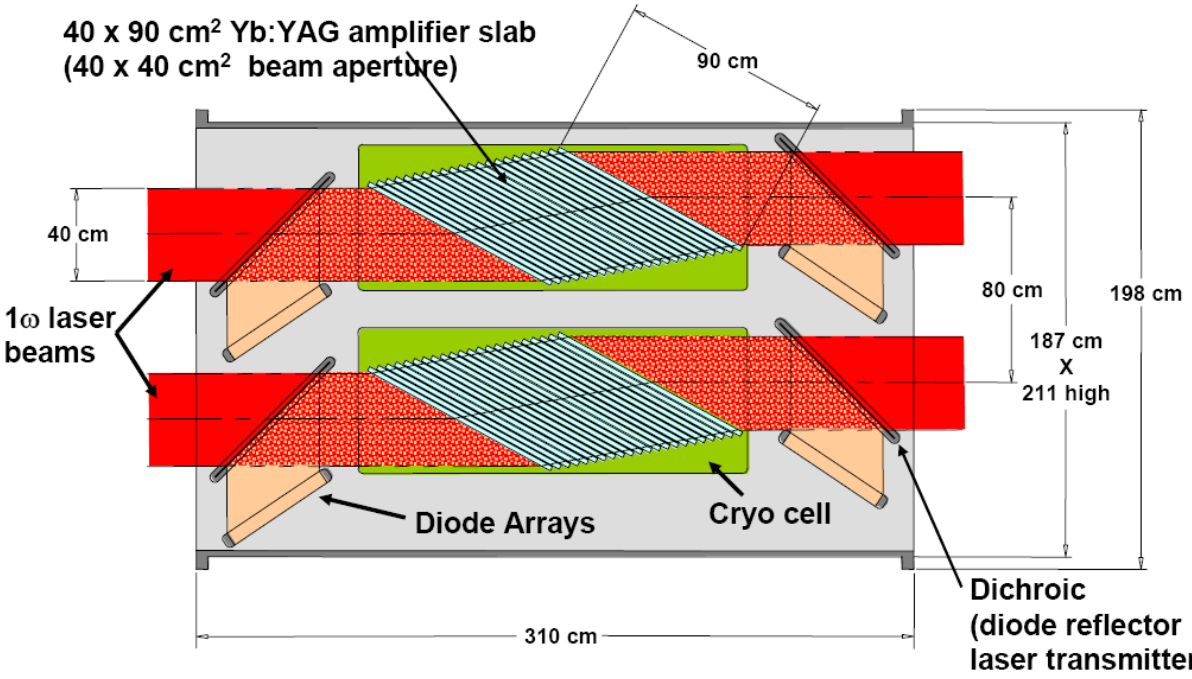

Fig. 1.2.4.7 Closely spaced Yb:YAG slabs yield very compact amplifier modules and enable the elimination of the intra-cavity vacuum spatial filters required by the other systems (Yb:S-FAP and Nd:Glass).

100K, the system behaves as a normal four-level laser system, population being frozen out of the terminal laser level. The important conclusion here is that the 100 K Yb:YAG system is projected to be at the same or even better efficiency than the room temperature Yb:S-FAP and Nd:Glass systems, even accounting for the consumed power that will be required to manage the Yb:YAG slabs at 100 K. One of the remaining issues with the Yb:YAG system is how to best separate the heat deposited in the edge claddings from the heat that is to be removed from the slab faces which are held at low temperature. It is extremely advantageous to remove the heart from the edge claddings at room temperature, as heat removal at cryogenic temperatures is less efficient. With these efficiency considerations, and the extremely rapid progress being made in transparent optical ceramics by many groups world wide, the ceramic Yb:YAG system viability comes down to a question of capital investment for the required cryo-cooling system, and how strongly this impacts the final cost of electricity.

To further understand the tradeoffs of each of the systems studied here, facility designs using a 48 port chamber were conceptualized. These facilities were strongly influenced by the NIF as shown in 1.2.4.8. In addition to the 48 port chamber, much of the switchyard and the use of LRU's leveraged what has already been demonstrated on NIF. The facilities for the three systems are compared side-by-side in Fig. 1.2.4.9. As seen there, the Yb:YAG based beam lines enable the smallest footprint for a facility, due to the close packed amplifier configuration and elimination of a transport spatial filter within the laser cavity, as already discussed. The next phase of this program will evaluate costs and risks associated with the three options outlined here, and perhaps consider other options as well.

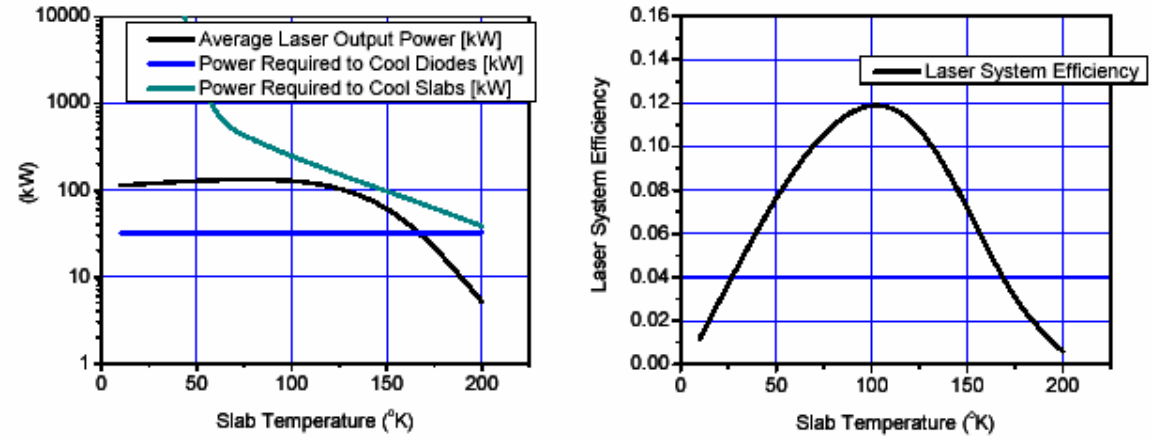

Fig. 1.2.4.8 Yb:YAG laser performance is temperature dependent and optimizes near 100 K. Curves on the LHS show how the power required to cool the laser slabs and the laser output change as temperature is varied. The curve of the RHS rolls up this analysis and shows overall laser system efficiency (including the power required to cool the laser slabs) as a function of slab temperature. Surprisingly, even including the additional power required to manage the thermal environment of the slabs at 100 K, the Yb:YAG system is efficiency competitive with the other two room temperature systems considered within.

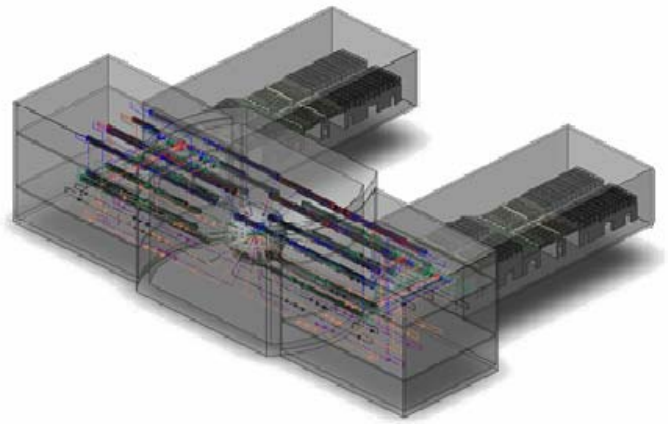

Fig. 1.2.4.9 Each of the three designs being evaluated was assumed to use a 48 port chamber geometry, leveraging the engineering already completed for the NIF system.

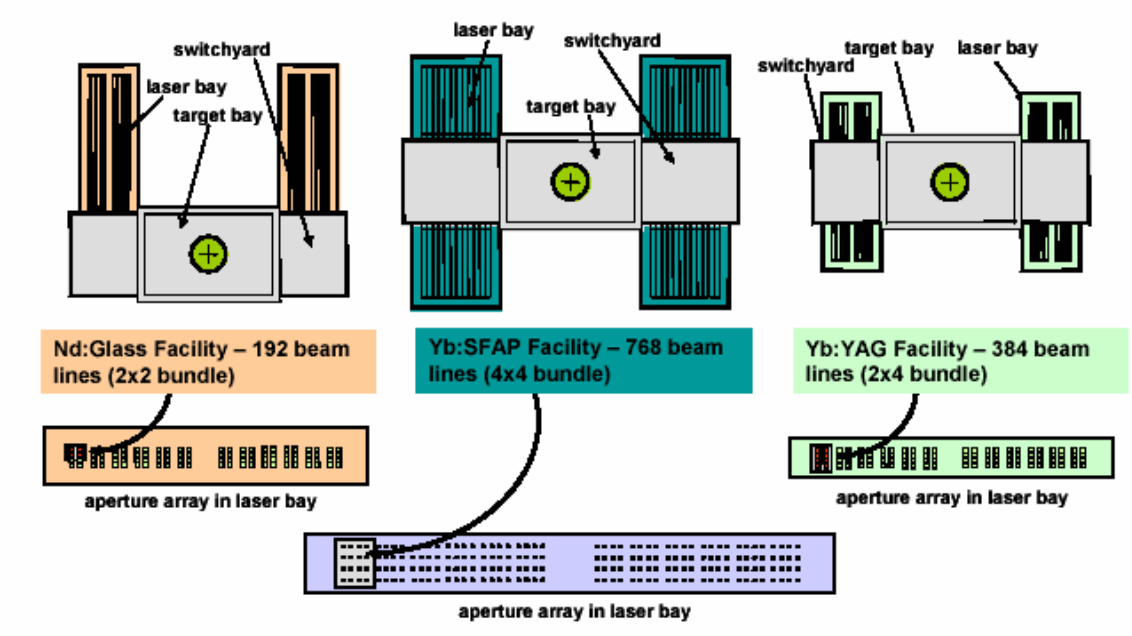

Fig. 1.2.4.10 Each of the three systems being investigated was used to scope and size a facility with target chamber. Shown above are the configurations we adopted for the Nd:Glass, Yb:S-FAP, and Yb:YAG options. The Yb:YAG system had the smallest facility size .

1.3 Advanced Technologies

Develop broadband injection laser with temporal and spectral capabilities. Design, build and demonstrate frequency conversion hardware and do integrated tests at 2ω on the Mercury Laser. Perform offline testing of deformable mirror technology.

1.3.1 Front End Laser Development with Spectral Sculpting

The front end laser provides a temporally and spectrally shaped pulse that is injected into the main Mercury laser system for amplification. The existing narrow band front end in the Mercury laser is sufficient to meet near-term project goals. The development activities on the new broadband front end are centered on providing a beam that can support up to 1 THz of spectral bandwidth on the beam. The goal for FY2005 was to complete the construction of the final two LMA fiber amplifiers and begin the construction of the Multipass Ring Amplifier (MPRA). Development of the controls and diagnostics system for the front end was also scheduled to occur in parallel with the hardware buildup.

Construction of the remaining two LMA fiber amplifiers was successfully completed. The large mode core geometry was chosen to reduce the accumulation of non-linear phase aberrations caused by propagating a spectrally-shaped, microJoule level pulse through a long length of dielectric material (the fiber itself). Figure 1.3.1.1 shows a representative picture of the LMA fiber amplifiers. The fully integrated fiber portion of the front end performed as predicted in that the output energies met or exceeded the design requirements of 400pJ, 100nJ and 30μJ (LMA1, LMA2 and FFA respectively). Figure 1.3.1.2 shows a plot of the output energy of each amplifier as a function of drive current to its pump diode.

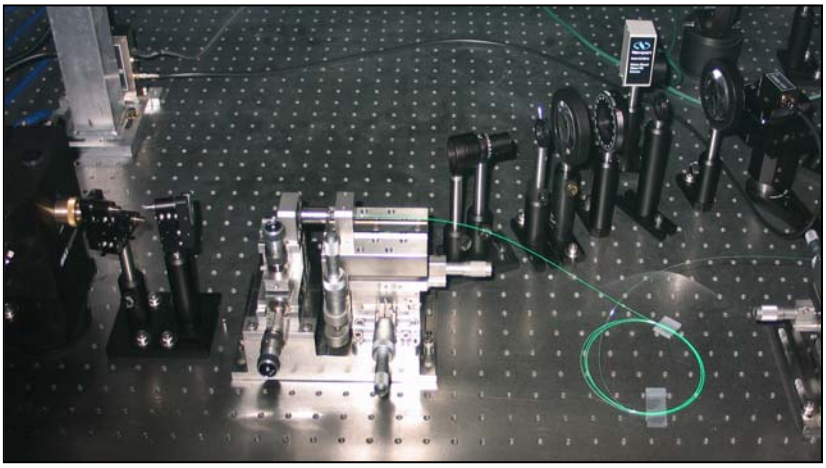

Figure 1.3.1.1 LMA fiber amplifier

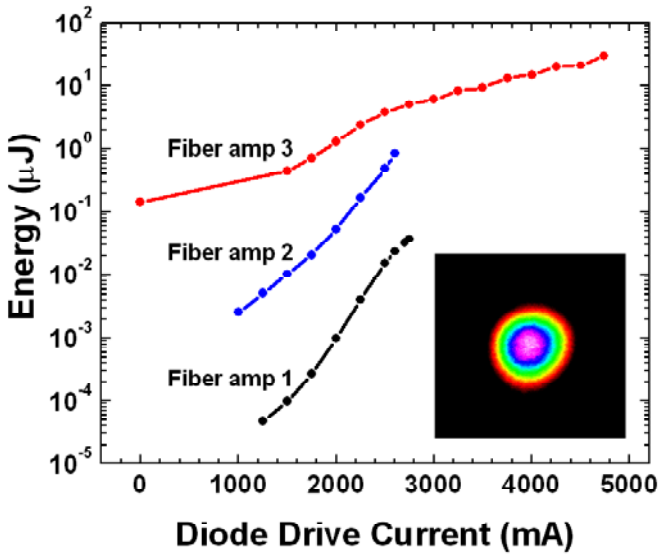

Figure 1.3.1.2 Fiber system energy performance data with output mode quality (inset)

Construction of the MPRA was started in FY2005. This involved building two small amplifier modules based on the Mercury amplifier design. The MPRAs utilize the same diode tiles, pump delivery scheme and Yb:S-FAP gain medium as the main amplifier. Figure 1.3.1.3 shows a picture of an assembled MPRA unit. The ring amplifier was aligned and activated for a low energy demonstration and to validate the models used to predict the performance of the MPRA.. Figure 1.3.1.4 shows the performance of the system during the low-energy validation experiment. Gain measurements were shown to meet requirements.

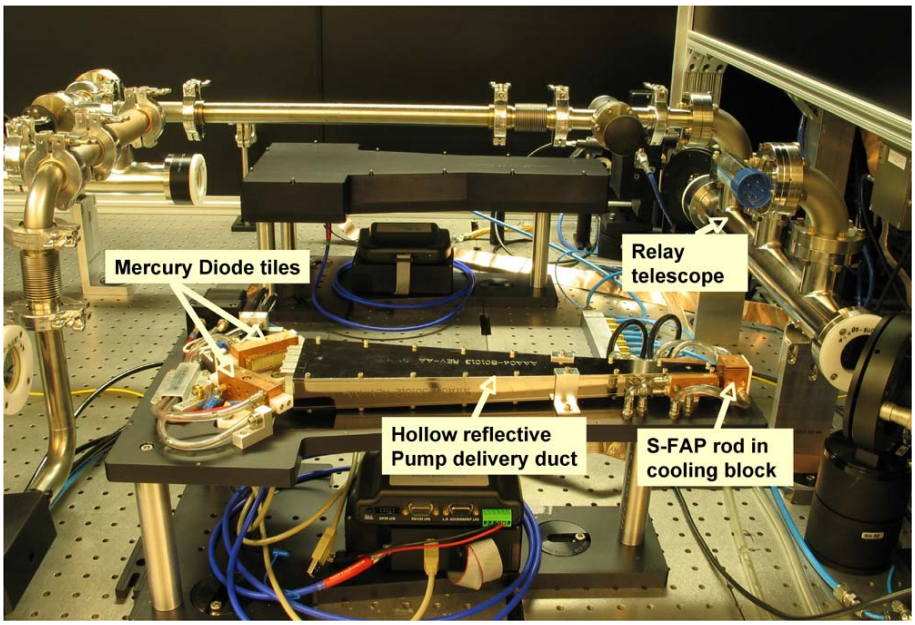

Figure 1.3.1.3 Multipass ring amplifier head.

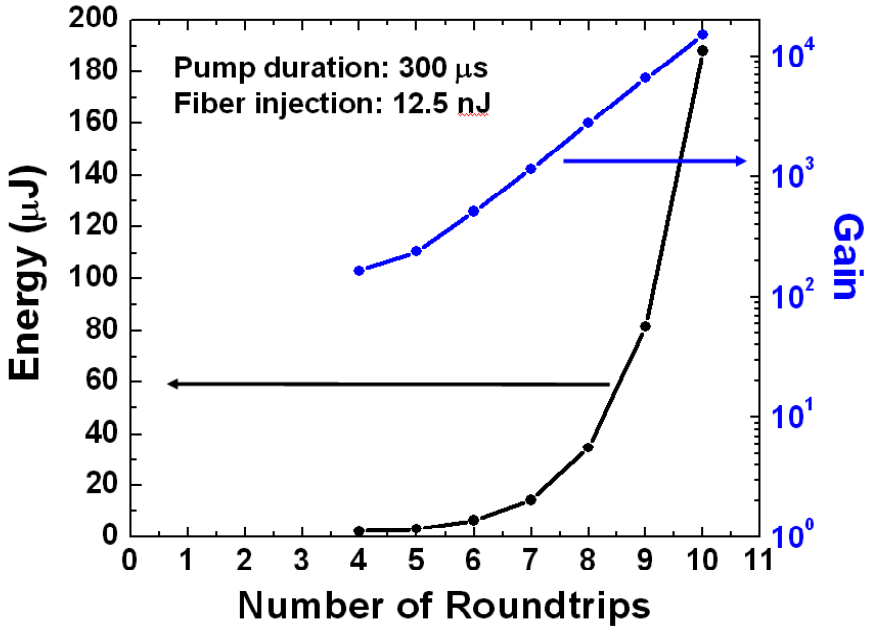

Figure 1.3.1.4 MPRA Output energy during the low-energy validation experiment

The controls and diagnostics system were expanded to include the LMA fiber amplifiers and MPRA systems. Diagnostics were added between to enable in situ monitoring of the fiber system, the phase modulator microwave pulse parameters, oscillator wavelength, and output temporal pulse. In addition several control system features were added such as a new timing system, temperature control on each fiber amplifier diode, and pump control for the MPRA heads.

A distributed architecture was implemented to allow for future growth of the system and yet be compatible with the existing controls architecture on the main system. The front end control system ties six computers that are networked for information sharing. A user interface code was developed to retrieve and display information form each computer for the operator.

1.3.2 Frequency Conversion

Mercury is currently in the process of system activation which, broadly speaking, takes place in two stages. The first stage, recently completed, has delivered 55 J at an average power of 550 W (10 Hz, 15 ns). The second stage will deliver 100 J with an average power of 1000 W. Even though the thermal loading on the nonlinear optical crystals is typically 100 times lower than the thermal loading on the gain medium, the need to maintain the phase velocities of the infrared and second harmonic light within the crystal to a small fraction of a wave is complicated by the relatively large value of the thermal change in the refractive indices. Even a modest temperature rise of a few degrees can result in significantly reduced conversion efficiencies. We are implementing a two-tier strategy for frequency conversion technology development: a low-risk baseline and a moderate risk-high payoff path. Currently the Yb:S-FAP gain medium is cooled via a recirculating system involving gas cooling with high-speed helium. Our 'baseline' frequency conversion cooling technology employs a sapphire heat spreader concept to allow for more flexibility in crystal thickness and crystal geometries for the initial materials characterization. For the frequency conversion crystal we have tested two materials:

DKDP whose growth to 40 cm apertures has already been demonstrated by the National Ignition Facility and YCOB, a crystal with very favorable thermo-optic characteristics compared to DKDP, which can potentially be scaled to apertures of 20 cm.

Currently, the Yb:S-FAP slabs are separated by 1 mm helium flow channels. The total heat removed from each crystal is on the order of 35 W with a thermal loading of approximately 2 W/cm^2. This gas cooling technique has the ability to scale to multi-kilowatt apertures. In contrast to the gain medium, nonlinear optical processes are elastic processes, with the thermal load arising strictly from the residual linear and nonlinear absorption in the crystal. Typical absorption coefficients for transparent crystals are on the order of 0.0025/cm, leading to an average power loading of 0.01 W/cm^2 on the Mercury 4.5 cm x 7.5 cm aperture beamline. These extremely modest thermal loads lead to temperature gradients of 2-3 degrees C in the nonlinear optical crystal. Nevertheless, this gradient can lead to thermal dephasing (reduced conversion efficiency) or thermal fracture. The small amount of heat that needs to be removed by the cooling system is relatively modest compared to the gain medium, and requires a significantly lower velocity of the helium gas. However, an adaptation of the current gas cooling technology for frequency conversion would require modifications to introduce angular tuning capability. Frequency conversion crystals require pointing adjustability. A typical pointing specification for critically phase matched crystals is 250 μrad. The difficulty is that the typical vendor orientation capability is on order of 17,000 μrad (+/- 0.5 degrees) thereby requiring the need to individually rotate the crystals with respect to the beam propagation direction.

Although the gas-cooling technology has the advantage in that it is well developed, we require more flexibility in our experiments with the crystal thickness and conversion geometries. Therefore, another technology has been commissioned, which relies on a highly thermally conductive and transparent substrate for cooling. We have chosen sapphire as the substrate since it is widely used as an optical window and has a relatively high thermal conductivity (0.3 W/cm/K) The frequency conversion cooler concept close couples the crystal to the sapphire plate (through a 30 micron air gap). Thermal modeling shows the sapphire face-cooled technology will scale to the required 20 cm aperture. The gas cooling and the heat spreader concepts are schematically shown in Figure 1.3.2.1.

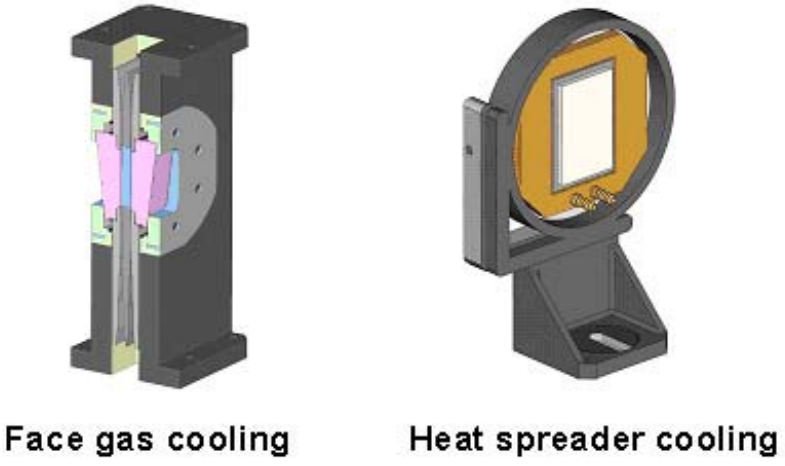

Figure 1.3.2.1 A heat-spreader cooling concept has been implemented (on the right) to manage the modest thermal loads present in the frequency conversion crystals.

We choose our frequency conversion crystals based on the ability to perform second

and third harmonic generation of 1047 nm with intrinsically low absorption. Of the commercially available crystals (DKDP, LBO, KTP, BBO, GdCOB, YCOB) DKDP and YCOB are chosen as the "baseline" and "advanced-concept" converter crystals, respectively. DKDP is a crystal with over 30 years of development effort with well-characterized material parameters such that the thermo-optical performance characteristics of DKDP can be reliably modeled. However, DKDP exhibits a relatively low fracture temperature (less than 10 ^{o}C), requiring the use of multiple plates to minimize thermal gradients. Recently, the nonlinear optical coefficients of two new oxyborates have been characterized. We are beginning to supplement the knowledge regarding the long-term reliability of these crystals for use as harmonic generators. YCOB has a significantly larger thermal acceptance (> 10x) and fracture strength (10x) than DKDP. Most importantly, large aperture growth of YCOB has been recently demonstrated, producing 7.5 x 25 cm boules. The growth efforts are summarized in Figure 1.3.2.2(a), showing a large aperture boule with only a whisper of veiling near the bottom. From these boules we have fabricated full aperture (4.5 cm x 8.5 cm), thick (1.58 cm), defect free plates of YCOB for the initial frequency conversion demonstration.

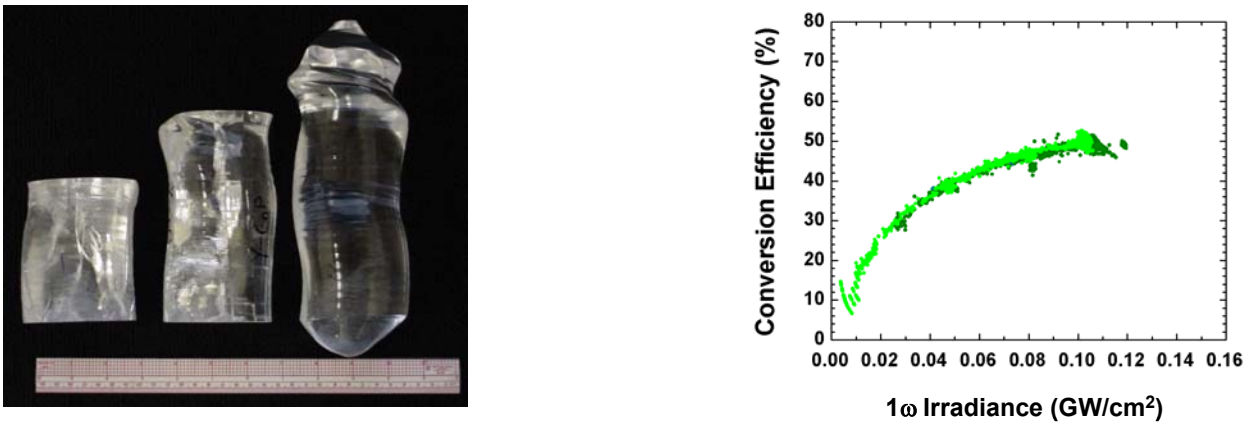

Figure 1.3.2.2 left) We fabricated 5.5 x 8.5 x 1.58 cm slabs from the YCOB boule on the left, grown at Crystal Photonics, Inc. right) We obtained 50% conversion using a single, uncoated, YCOB plate (22.5 J, 10 Hz).

Thermal management by gas face-cooling has been shown to be scaleable to the 20-30 cm aperture for thermally loaded Yb:S-FAP. Potential limitations include the gas temperature rise between the time the gas first picks up heat from the lasing medium or nonlinear optical crystal and as it exits past the crystal. The modest heat loading from the gas-cooled frequency converter does not impose any such aperture constraints. Due to the small amount of heat that needs to be removed from the frequency conversion crystals, this transverse thermal gradient (transverse to the beam propagation direction) is less than 1/10th the longitudinal gradient (gradient across the thickness of the crystal) and has minor impact on the conversion efficiency. The side-cooled sapphire has limitations due to the need for heat transport across the sapphire optic before it is transferred to the cooling medium (water). Nevertheless, thermal modeling of the system indicates high conversion efficiency can be obtained, even with relatively large (20 cm) apertures. We have tested the cooling concept utilizing a single 1.5 cm thick DKDP plate faced cooled by a 5 mm thick CaF_2 plate separated by a 30 micron air gap. We found that at an incident average power of 450 watts, the DKDP frequency converter did not display any sign of thermal dephasing during the 30 minute test run. Given the low drive, multiple (4) DKDP plates would be required for high conversion efficiency (greater than 50%). The single plate of DKDP

had an conversion efficiency of approximately 12%, in agreement with modeling.

Utilizing a full aperture YCOB plate, the output of the Mercury laser (55 J, 10 Hz, 15 ns) was frequency converted, generating a record 227 W of average power at 523.5 nm. The beam was image relayed to an uncoated, side-cooled YCOB crystal with a thickness of 1.58 cm. A pictorial summary of the YCOB boule development over FY2005 is shown in Figure 1.3.2.2 (right). The experimentally measured conversion efficiency, (Fig. 1.3.2.2(left)), matched the expected theoretical performance including the angular acceptance of the crystal. The frequency conversion assembly was operated for a total of 30 minutes with no sign of optical damage (surface or internal). As the laser is brought to the higher output energy, we will utilize a YCOB doubler that is optimized for the higher fluence (a thinner crystal with a larger angular acceptance), with an expected conversion efficiency approaching 80%.

We are implementing a two-tier strategy in activating frequency conversion system for the Mercury laser. We have chosen for our baseline cooling technology a heat spreader concept and have tested the thermal performance of DKDP with this technology. As a moderate risk – high payoff strategy we have modeled the thermal performance of a face and side cooled YCOB frequency conversion crystal. We have achieved a record average power performance from a side cooled YCOB crystal, producing an average power of 225 W at a conversion efficiency of 50%.

1.3.3 Advanced Wavefront Control

High average power operation of the Mercury laser will require implementing active wavefront correction optics. In an effort to accurately specify the wavefront correction system needed, recent measurements of the system wavefront were analyzed using Legendre decomposition. Legendre decomposition projects the wavefront into Legendre polynomials (similar to Zernike polynomials for circular apertures), which can be examined to determine the distribution of the spatial frequency content of the wavefront aberration. Figure 1.3.3.1 shows the measured thermal wavefront (left) and the corresponding Legendre polynomial projection (right). The Legendre polynomial projection shows that the thermal wavefront is dominated by low order spatial frequency content, mostly second order (power) terms. The Legendre projection analysis indicates that a wavefront corrector capable of correcting 2^{nd} order (width) by 4^{th} order (length) would be adequate. Since it takes nominally 2 actuators to correct for each order of aberration, this implies that the wavefront corrector would need to have at least 4x8 actuators. The experimental data also indicated that up to 4 waves of low order aberration (mainly power, with spatial resolution < 0.5 cm^{-1}) could be expected at each pass. The large corrections (> 10 waves) required makes pre-correcting the injection beam extremely difficult to implement. As a result, it was decided that the wavefront correction will take place after two passes through the amplifier at an end mirror location. Correcting the wavefront during the amplification process also adds some complications such as the need for higher damage thresholds and requiring the corrector to experience two passes of the laser pulse.

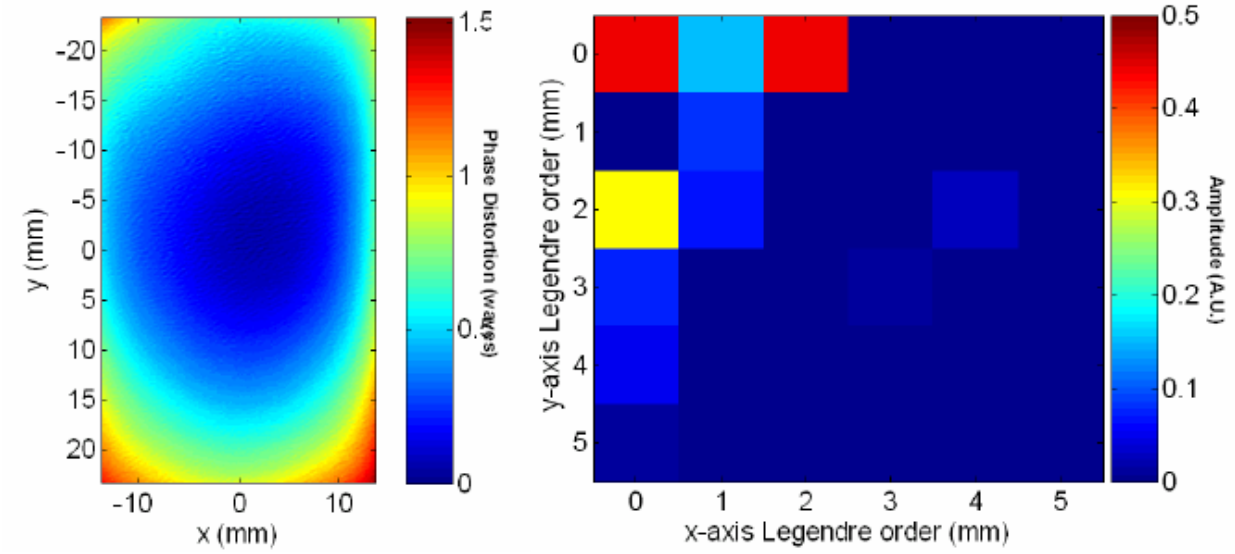

Figure 1.3.3.1 Thermal phase map (left) and Legendre polynomial decomposition projection (right). The primary phase on the beam consists of 1.5 waves of correctible spherical power.

A design specification was drafted based on the thermal phase data as well as theoretical modeling (see Table 1.3.3.2). Commercially available wavefront corrections systems were scoped in terms of:

1. Fully proven commercial systems
2. Short lead time
3. High cost benefits
4. Fully integrated system

A vendor was found that met all of the above criteria. A 100-mm diameter bimorph deformable mirror (DM) with 5 x 8 (41 total with an additional focus actuators) actuators with spacing of 10 mm has been designed (see Figure 1.3.3.3) and will be placed in the Mercury laser system such that it will reflect the beam after passes 1 and 3. An advantage of the bimorph deformable mirror is that the outer actuator can compensate for low order distortions of up to 20 waves. Damage tests of the coating witness sample showed no damage up to 10 J/cm^2 (max. expected fluence is 1.5 J/cm^2). The reflectivity of the coating is measured to be 99.98%, this implies very little energy will penetrate into the substrate. As a result, cooling of the DM is no longer a concern although a water-cooled DM is also available. Extensive modeling of the DM's performance using the response matrix of the deformable mirror indicates that a residual wavefront with RMS of 0.03 waves is possible with the non-even influence function of the system due to the beam inversion between the 1st and 2nd reflections on the DM (see Figure 1.3.3.4).

Table 1.3.3.2 Specification for Mercury Wavefront Correction System.

	Mercury Specification	Vendor Capability
Active Aperture [mm]	45 x 75	100
Max. correction (PV) [waves]	4	12
Max. correction (RMS) [waves]	0.1	0.05
Actuator Spacing [cm]	1	0.8 – 1.5
Wavelength [nm]	1047	1047
Energy [J]	35	35
Damage threshold [J/cm^2]	2	>10
Resolution [sampling points]	128 x 128	300 x 300
Repetition Rate [Hz]	3	10
Sensitivity [waves]	0.05	0.02
Dynamic Range [waves]	0.01 – 10	0.005 to 150
Warranty/Service Contract	Yes	Yes

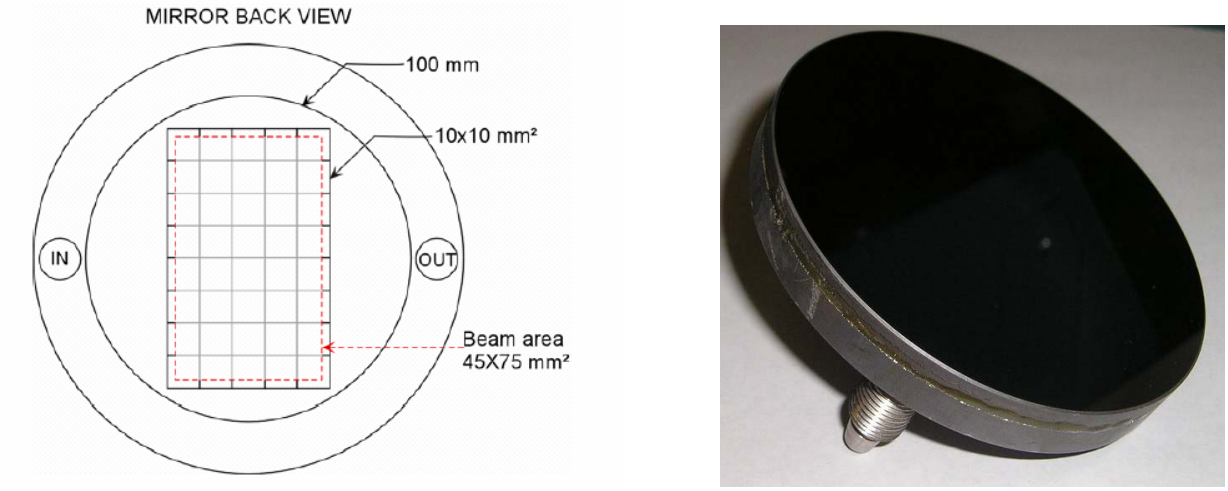

Figure 1.3.3.3. Schematic of bimorph deformable mirror (DM) with 41 actuators.

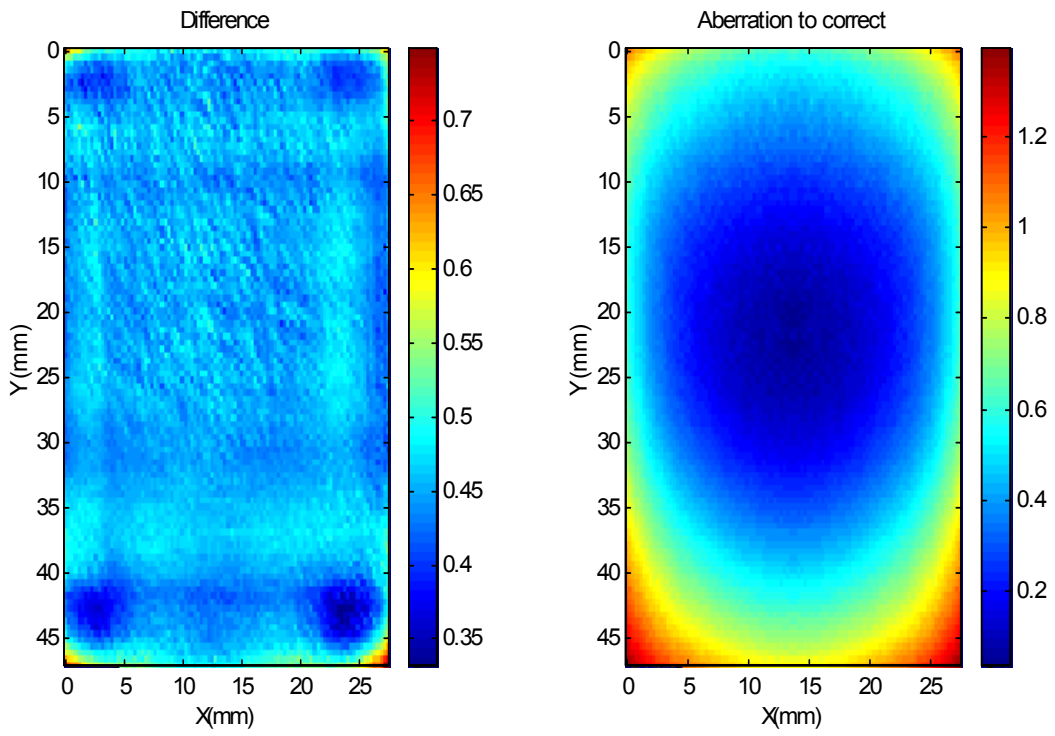

Figure 1.3.3.4. Modeling results showing the aberration to be corrected (left) and the possible residual wavefront error (right, RMS = 0.03 waves) after correction from a 5x8 actuator DM.

2.0 Chambers

The Chambers tasks include activities related to the chamber itself and broader topics dealing with integration of the chamber with other power plant subsystems. Task 2.1, Chamber Response and Safety and Environment, includes three subtopics this year: 1) development and utilization of the RadHeat code, 2) safety and environmental assessment of the lithium cooled chamber concept, and 3) shielding analysis for the magnetic cusp chamber concept. Task 2.2, Chamber Scaling and Scoping Studies, covers work on systems modeling and analysis for laser driven IFE power plants.

2.1 Chamber Response & Safety and Environment

The FY2005 objectives for Task 2.1 were to 1) continue with development of the RadHeat code, 2) provide safety and environmental support to design activities, and 3) design the shielding layout for the magnetic cusp protection scheme. These objectives were met, and the results are summarized in the following subsections.

2.1.1 RadHeat Code

Our FY2005 tasks were to:

- Transition from finite-difference to finite-element methods for solving the heat diffusion equation,
- Implement stress-strain models within RadHeat, and
- Analyze radiation shielding layout for the "droopy cusp" magnetic protection scheme.

RadHeat is a one-dimensional, transient heat transfer code that can be used to analyze a variety of inertial fusion relevant issues where rapid, pulsed heating of multilayered targets by penetrating radiation is a concern (see LLNL document UCRL-SM-208820). It uses an implicit finite difference discretization of the heat diffusion equation and draws upon user generated tables describing temperature dependent material properties, ion stopping tables, and a host of other data to calculate solutions to problems impossible to solve analytically.

Greater simulation accuracy could be obtained by shifting to a finite element method for solving the fundamental heat flow equations, and this was proposed for FY2005. It was realized, though, that efforts would be better spent formulating and implementing better refined stress-strain models rather than overhauling the core of the code for a marginal gain in computational speed.

Useful elastic stress, strain, and deflection physics were added to the code in FY2005 setting the foundation for more realistic elasto-plastic models to be added in the near future. These upgrades have been usefully employed for several tasks. For instance, it was shown that an aluminum grazing incidence metal mirror (GIMM) final optic directly exposed ion from the fusion target will experience a peak compressive thermal stress of 70 MPa due to the temperature spike generated from this radiation. This may be in excess of the material's plastic yield limit (see Figs. 2.1.1.1 and 2.1.1.2). This would be catastrophic since subsequent cooling would put the mirror's surface in tension and very quickly cause it to form stress-relieving cracks that would degrade its optical performance. This realization further emphasizes the need for some form of ion debris mitigation scheme to spare these critical components from direct exposure from target output.

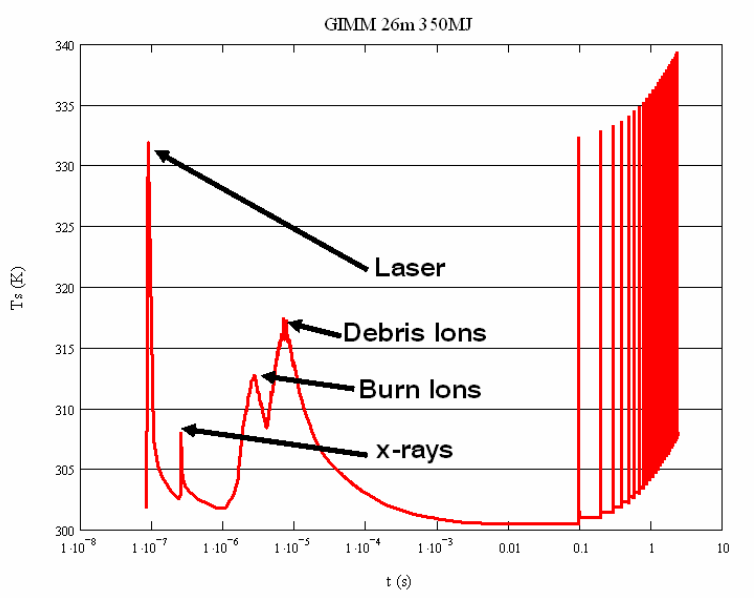

Fig. 2.1.1.1. The surface temperature (K) response of an aluminum grazing incidence metal mirror (GIMM) at 26 m from chamber center to the 350 MJ HAPL direct-drive target. The radiation effects causing the various temperature peaks are pointed out.

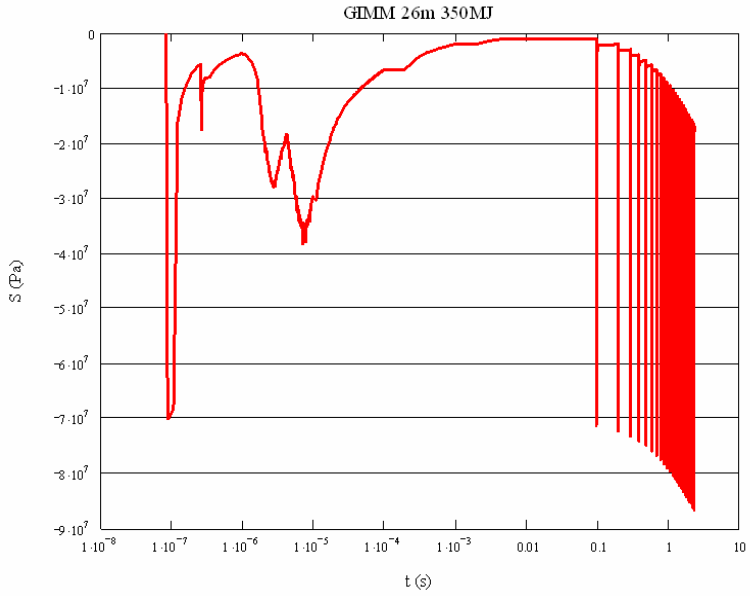

Fig. 2.1.1.2. The transient compressive stress (Pa) that will be experience at the surface of a GIMM irradiated by the 350 MJ HAPL direct-drive target based on an elastic stress model implemented in RadHeat. A more detailed elasto-plastic stress model will show effects of plastic deformation and hysteresis for multiple pulse simulations.

2.1.2 Safety & Environment

Regarding the safety issues associated with liquid Li, we completed a safety assessment including an overview of potential chemical reactions, a literature search on past liquid metal systems and previous fusion designs using Li, and a preliminary accident analysis for the HAPL reactor design.

There are critical safety issues to be addressed when handling liquid Li due to the chemical reactivity of Li with air, water and other substances. The direct energy release from such chemical reactions could lead to high temperatures and pressures in the chamber and surrounding structures causing facility damage and accident propagation. Furthermore, the indirect energy release from secondary chemical reactions involving initial reaction products (i.e., Li-H_2O reaction produces H_2 gas which may lead to hydrogen combustion) could generate additional accident sequences. The dominant issue in an accident scenario with Li chemical reactions is the mobilization of tritium and activated structural materials. Therefore, it will be critical to minimize the risk of chemical reactions.

The potential chemical reactions of Li with air are:

$$6Li + N_2 \rightarrow 2Li_3N + 69 \text{ kJ/mole-Li (at 500 °C)}$$
$$4Li + O_2 \rightarrow 2Li_2O + 302 \text{ kJ/mole-Li (at 500 °C)}$$

If we consider that air is 79% N_2 and 21% O_2 and that all the Li inventory in the HAPL cooling system (~500 tonnes total) is available to react with unlimited air, the potential chemical energy released could be up to 7500 GJ. Considering that it only takes ~ 1 GJ to melt 1 ton of steel, this would result in an excessive energy release. Therefore, a cover gas (Ar, He) should be used in the reactor building. Given that liquid lithium also reacts exothermically with CO_2, the use of CO_2 as a cover gas is not a good option. The former estimate is based in the simplistic assumption that all the liquid Li will react with an unlimited supply of air. For a more realistic estimate, thermal-hydraulics calculations are needed to better address the consequences of accidents involving a Li leak with simultaneous air ingress event.

Liquid Li also reacts exothermically with water through the following reactions:

$$\text{Excess Li:} \quad 2Li + H_2O \rightarrow Li_2O + H_2 + 160 \text{ kJ/mole-Li (at 25 °C)}$$
$$\text{Excess } H_20: \quad 2Li + 2H_2O \rightarrow 2LiOH + H_2 + 200 \text{ kJ/mole-Li (at 25 °C)}$$

Table 2.1.2.1 shows the stored chemical energy and potential H_2 generation per kg of Li and also in the total power plant inventory. Using the ITER limit of 10 kg of H_2 generation, the water spill should be limited to a maximum of 90 kg. As a consequence, we recommend avoiding the use of water in the reactor building..

When liquid lithium contacts concrete above 100 °C, it will first react with the water vapor released from the concrete and with the chemically bound water that is released above 200 °C. At higher temperatures, it will also react with other concrete constituents, in some cases exothermically. As a consequence, contact between Li and concrete should be minimized by using steel liners over the concrete surfaces, catch pans, and suppression tanks as needed.

We also performed a literature search of past working Na/Li systems to try to learn some lessons from previous operating experience. In the case of liquid metal fast breeder reactors, we found that most of them had cost and non-proliferation issues that overshadowed the liquid metal safety issues. Some of them had some incidents with release of liquid Na and consequent fires,

but even in the most severe cases (Monju, Superphenix), neither injuries nor radiation exposures were recorded.

Regarding past fusion designs using liquid Li, we have studied the designs of UWMAK-I (1974), UWMAK-III (1976), BCSS (1983), HYLIFE-I (1985), ESECOM– VLi TOK (1989), and ARIES-RS (1996). These designs used liquid Li with inventories ranging from 270 tonnes in ARIES-RS, up to 870 tonnes in the case of HYLIFE-I. The tritium inventories range from 100 g in ARIES-RS (cold trapping with added protium extraction) up to 1 kg in HYLIFE-I (molten salt extraction). The common safety features of all these included: multiple containment to liquid breeder release, segmented Li inventory, inert cover gas, steel liner over concrete, minimized use of water or no water at all, and high heat capacity materials (i.e. steel balls) used to cool down potential spills.

We completed a preliminary safety assessment of the HAPL chamber using liquid Li. Neutron transport and activation calculations were performed for a Li blanket in a 10.5 m radius chamber. Two operational scenarios were considered: 5 Hz (FW lifetime = 10 yrs) and 10 Hz (FW lifetime = 5 yrs). We found that the FW afterheat in the case of 10 Hz increases by a factor of ~2. The Waste Disposal Rating (WDR) is equivalent in both cases, and WDR < 0.2 for both the W armor and the FS blanket structures. Also, we used the heat transfer code CHEMCON to simulate a loss of flow accident (LOFA) and assess dissipation of afterheat during the accident. We found that the decay heat rapidly transfers through radiation to cooler structures (confinement building). For the chamber design with oxide-dispersed-strengthened (ODS) steel, the starting temperatures are higher, but the same trend can be observed. In the case of 10 Hz operation, increased afterheat results in a slower transfer, but it also decreases gradually due to radiation (see Figure 2.1.2.2).

Finally, a version of the thermal-hydraulics code MELCOR capable of assessing Li fires (developed by Idaho National Laboratory (INL)) was used to simulate a Li fire in the HAPL chamber. We found that even in the case of a major spill with simultaneous air ingress (300 ton spill and a 1-m diameter break in the confinement building), the temperatures of all the structures would remain below melting. In these circumstances, the maximum hazard would be the release of the tritium contained in the liquid Li as a consequence of the fire, and therefore, it is critical for the safety of the design to minimize the tritium inventory in the coolant loop. Possible approaches may include: gas recovery systems, getters, cold traps, and molten salt and permeation technologies. We estimated that in case of an elevated release and conservative weather conditions, a release of 200 g of tritium is enough to reach the 1-rem limit for no-evacuation. This dose would be 10× larger in case of ground release, and 10× smaller if typical weather conditions were assumed instead. It is strongly recommended that the tritium inventory in the coolant be as low as possible, ideally less than 100 g.

As a summary of this assessment, we conclude that the use of lithium as both the breeder and coolant is feasible; however, careful design must be utilized to decrease the risk from a lithium spill. Safety recommendations include: use an inert cover gas (Ar, He), avoid the use of water in reactor building, use liners over all concrete surfaces that could come in contact with spilled lithium, keep the Li inventory at low pressure and segmented, use multiple containment barriers to liquid Li release (e.g., dump tanks), use high heat capacity materials (i.e. steel balls) to cool down a spill, and minimize the tritium inventory in coolant to avoid radioactivity release in case of Li spill.

Table 2.1.2.1. Chemical energy and H_2 generation per kg of Li and in total Li inventory.

Reaction type	Chemical energy stored (GJ/kg-Li)	Total chemical energy (GJ)	Potential H_2 release (kg/kg-Li)	Total potential H_2 production (kg)
Excess Li	0.022	11,000	0.144	72,035
Excess H_2O	0.029	14,500	0.144	72,035

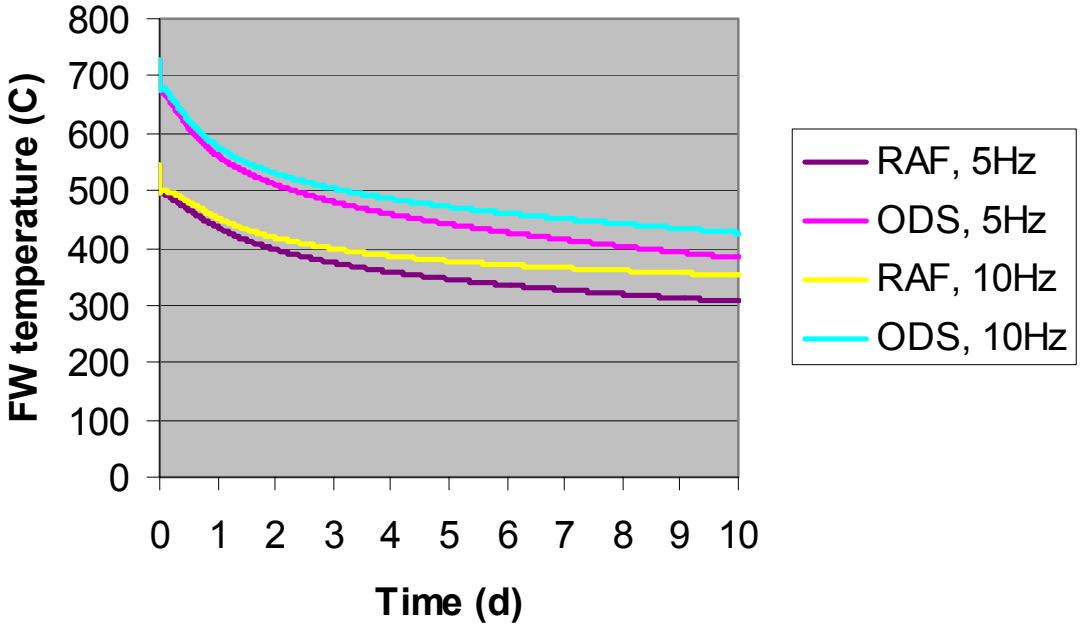

Fig. 2.1.2.2. Evolution of FW temperature during LOFA in baseline (RAF at 545 °C) and enhanced (ODS at 719 °C) cases at 5 and 10 Hz operation.

2.1.3 Shielding Analysis for Magnetic Cusp Chamber Concept

Our FY2005 task in this area was to analyze the radiation shielding layout for the "droopy cusp" magnetic protection scheme. Neutron transport and shielding calculations were completed for the coils needed to implement cusp magnetic protection of the first wall.

Figure 2.1.3.1 is a plot of the neutronics model used in the calculations without shielding. In estimating the lifetime of the magnets, limits of 100 MGy dose to the insulators and a fast neutron fluence of 10^{19} n/cm^2 to the NbTi superconductor were assumed. With these limits, the coil lifetimes would range from only 0.1 years to ~3 years without shielding.

To extend the lifetime of the magnets, radiation shielding was added. Note that the shielding design has not been optimized. Many opportunities exist for optimization of the shielding cost, thickness, mass, etc. Figure 2.1.3.2 shows the configuration with magnet shielding. With shielding, magnet lifetimes range from ~25 years for the top/bottom coils to ~70 years for the other coils. This suggests that additional shielding is needed near the poles, while it can be reduced near the equator.

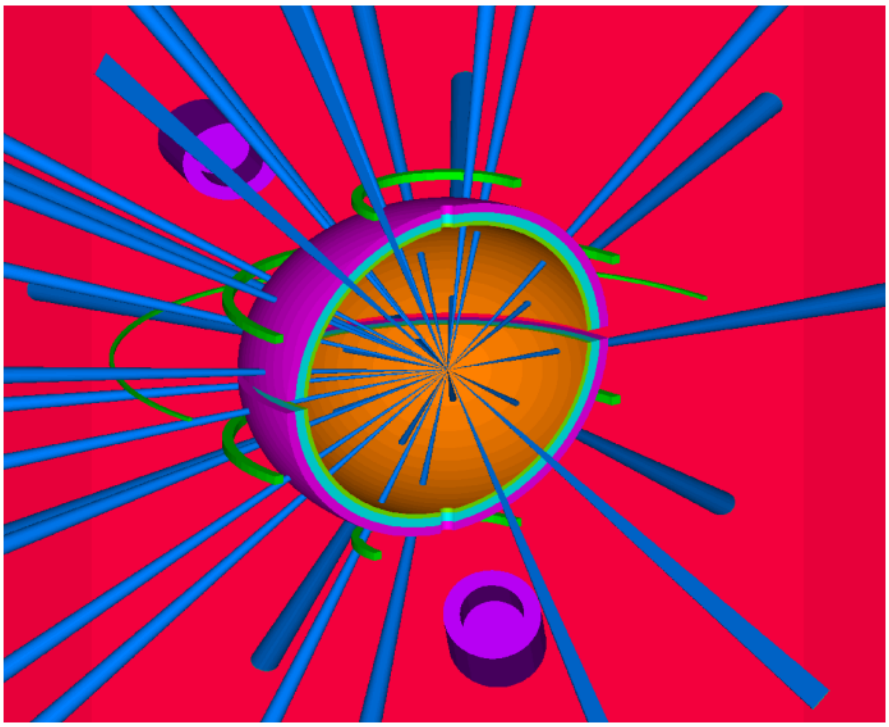

Fig. 2.1.3.1. A cutaway view of the neutronics model shows the spherical chamber and blanket, direct drive beams (blue), superconducting coils (green), and neutron dumps (purple).

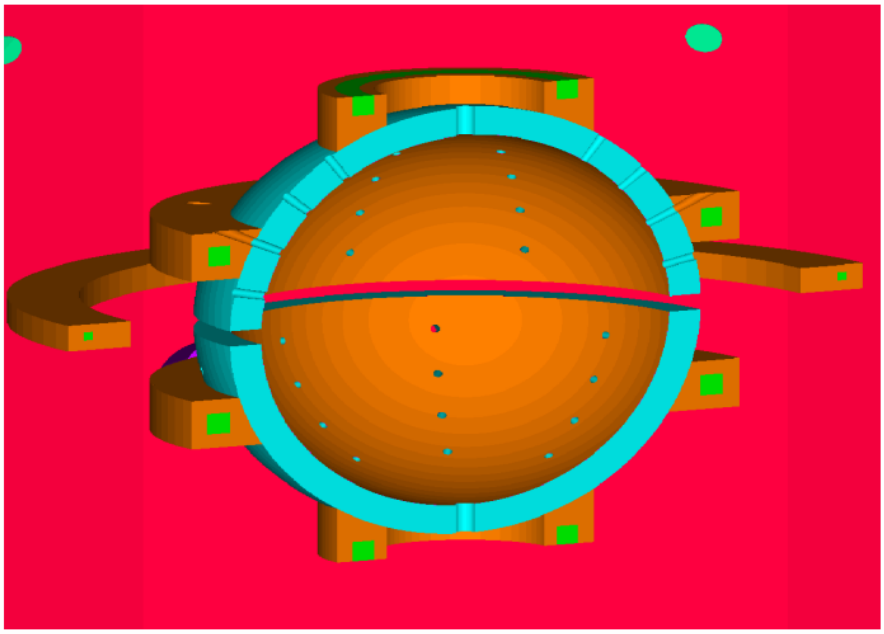

Fig. 2.1.3.2. A cutaway view of the second neutronics model shows superconducting coils surrounded by radiation shielding. The direct drive beams have been removed for clarity.

2.2 Chamber Scaling & Scoping Studies

The long-range goal of this work is to develop an improved, integrated systems modeling capability that includes current understanding of the physics, engineering and costing information for candidate drivers, targets, chambers, and power conversion subsystems. In FY2005, we completed and published scaling models for the Li-cooled chamber concept with a Brayton power cycle [1]. Updated target gain curves were also included in the systems model. Complete parametric studies assessed the impact of driver cost and efficiency on overall plant economics in order to provide some insight in this area. Key results from the driver scoping studies are highlighted here.

Base Case Assumptions for Driver Scoping Studies

For this analysis we used the power plant systems model previously developed for the Sombrero laser IFE plant design but substituted updated target gain curves and included driver cost and efficiency as parameters instead of calculated values. This work was reported at the June 2005 HAPL Project Meeting [1]. For the cases shown here, we held the net power of the plant at 1000 MWe and used the target gain curve for a 1/3 μm laser driver (frequency tripled DPSSL). Normalized cost of electricity (COE) is used as the figure of merit with results normalized to a case using:

Driver energy = 3 MJ
Target gain = 121
Yield = 363
Rep-rate = 7.2 Hz
Driver efficiency = 10%
Driver total capital cost = $500/J

As shown below, this point is near optimum for this combination of driver cost and efficiency.

Impact of Driver Cost on COE

Figure 2.2.1 show how the COE varies as a function of driver energy for three different driver cost assumptions, $250/J, $500/J and $750/J. Note that the middle value of $500/J is close to the result obtained by Orth for a DPSSL [2]. The curves all have a similar shape. At low driver energy, the COE is high due to low target gain resulting in high recirculating power fraction, which requires more gross electric power (and high capital cost) to meet the 1000 MWe net power output. The COE curves go through minima and then increase again at higher driver energies; this reflects the fact that beyond the minimum, the cost of achieving higher gain with a larger driver is not offset by reductions in the cost of the plant due to lower recirculating power needs. Comparing the three curves, we note that a $250/J change in the driver cost results in approximately +/- 12% change in the COE at constant driver energy (3 MJ). At $500/J the optimum driver energy is 2.5 MJ, but the COE is only slightly lower (1%) than the normalizing point at 3.0 MJ. To operate at 2.5 MJ, however, the chamber rep-rate would have to be increased to 10.8 Hz. Higher driver costs push the optimum point to somewhat lower driver energies, which correspond to higher rep-rates. For the $750/J case, the minimum COE occurs at a driver energy of 2.0 MJ and 14.7 Hz and is ~3% lower than at 3 MJ and 7.2 Hz.

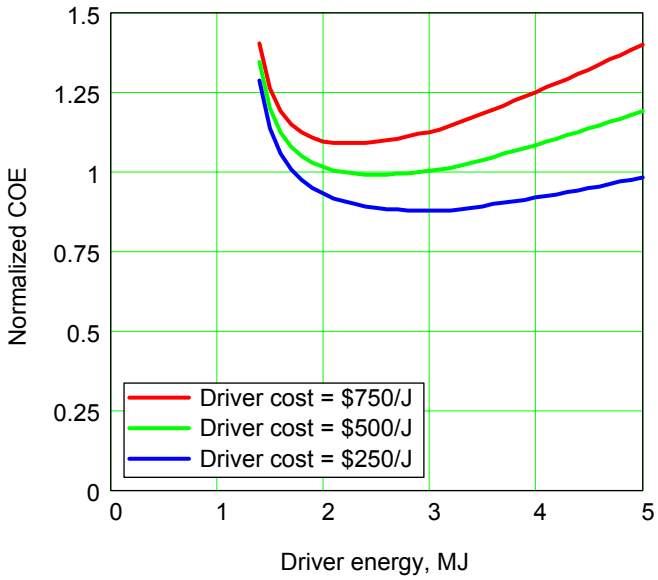

Fig. 2.2.1. Normalized COE as a function of driver energy with driver cost as a parameter ranging from $250/J to $750/J

Impact of Driver Efficiency on COE

Figure 2.2.2 plots the normalized COE as a function of driver energy for driver efficiencies of 5, 10 and 20%. At a constant 3 MJ, the COE with a 5% efficient driver is 13% higher than with a 10% efficient driver, while the COE with a 20% efficient driver case is < 5% better. Note that the optimum driver energy decreases with increasing driver efficiency, ranging from 2.1 MJ (14.1 Hz) at 20% to 3.3 MJ (7.3 Hz) at 5%. In all cases, however, there is a relatively broad range of driver energies (+/- 0.5 MJ) and corresponding rep-rates that give near optimum results (i.e., within a few percent).

Sensitivity Comparison

Figure 2.2.3 shows the sensitivity of the normalized COE to changes in the driver cost and efficiency for a fixed driver energy of 3 MJ. The COE is directly proportional to the driver unit cost at ~ 2.4% per 10% change in driver cost. Figure 2.2.3 clearly shows the importance of increasing driver efficiency particularly in the 5-10% region, with diminishing returns between 10 and 20%.

References for Section 2.2

[1] W. Meier, "Update on Systems Modeling for Laser IFE," UCRL-PRES-212978 (June, 2005). http://aries.ucsd.edu/HAPL/MEETINGS/0506-HAPL/poster.html

[2] C. Orth, S. Payne, W. Krupke, "A Diode-Pumped Solid-State Laser Driver for Inertial Fusion Energy," *Nuclear Fusion*, **36**, 75 (1996).

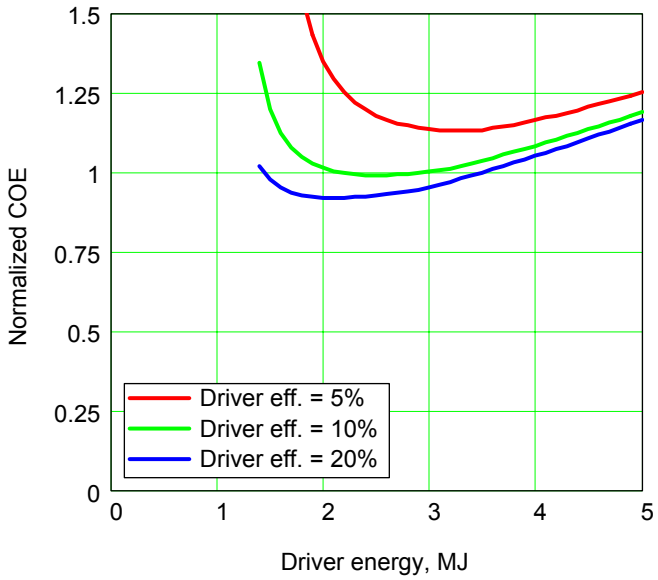

Fig. 2.2.2. Normalized COE as a function of driver energy with driver efficiency as a parameter ranging from 5% to 20%.

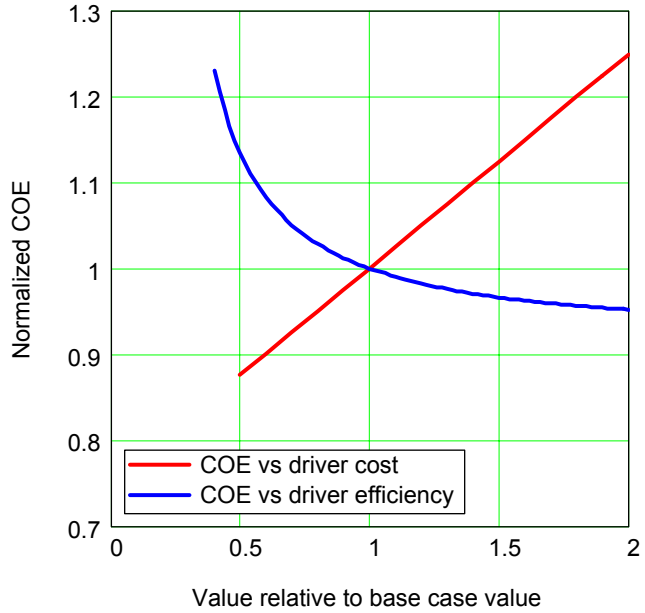

Fig. 2.2.3. Sensitivity of COE to variations (from ½ to 2×) in driver cost and efficiency relative to base case values ($500/J and 10%) at fixed driver energy of 3 MJ.

3.0 Final Optics

Our research in the area of final optics included two main parts in FY2005: irradiation studies of candidate optical materials and ion debris mitigation studies. Progress in these areas is discussed in the following subsections.

3.1 Irradiation Studies

Our FY2005 task for the irradiation studies was to continue ion and neutron irradiation tests of grazing incidence aluminum metal mirrors with emphasis on the threshold for ion implantation damage.

As reported last year, multilayer dielectric mirrors were irradiated with neutrons at Oak Ridge National Laboratory during FY2003. The samples were received at LLNL during FY2004. Unfortunately, the samples were severely scratched and post-irradiation reflectivity data could not be obtained.

Fortunately, it was possible to complete cross-sectional transmission electron microscopy (XTEM) for these samples. XTEM imagery shows interesting effects in the dielectric mirrors. Figure 3.1.1 shows an XTEM image of one of the 4ω mirrors. The dark regions are Al_2O_3, and the light regions are SiO_2. Note that Al_2O_3 layers show numerous clusters of bubbles and other defects. Significant crystallization is seen as well in higher magnification images. Prior to irradiation, bubbles were not observed and crystallization was minimal. Similar results were observed for the 3ω mirrors.

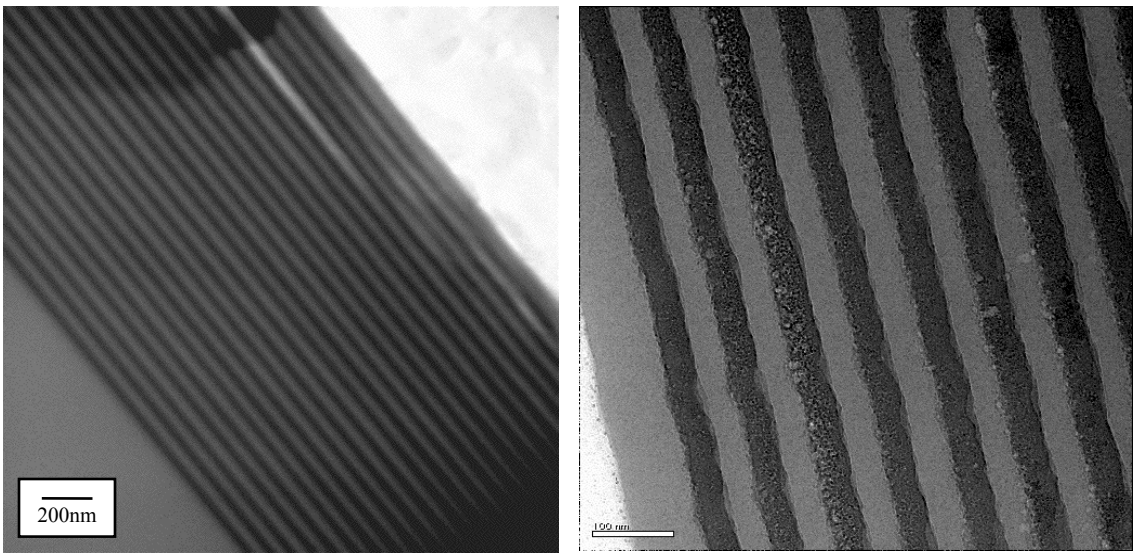

Fig. 3.1.1. XTEM images of a 4ω mirror show alternating layers of SiO_2 and Al_2O_3. The left image was taken of an unirradiated sample, while the right image was post-irradiation. Bubbles can be observed within the alumina layers of the irradiated sample. Note that the scales are different: the size bar is 200 nm in the left image but only 100 nm on the right.

It is unknown at this point whether or not the rippled layers and bubbles will have effects upon the laser reflectivity or damage threshold. Preferred multilayer materials will be identified and additional neutron irradiations will be completed. Subsequent reflectivity and laser damage experiments are planned.

Additional ion irradiations were conducted during FY2005. Although the IFE target output is pulsed, it is expected that ion damage to mirrors is driven by total fluence rather than flux. RadHeat calculations show that the expected temperature rise in aluminum GIMMs is only 10's of degrees. As a result, steady-state ion irradiations are appropriate. All implantations have been conducted with alpha particles, which are a major constituent of the target debris. Alpha energies of 3.0 and 0.5 MeV were used.

As reported in FY2004, the first round of ion implantations suffered from inadequate vacuum conditions. To rectify this, a cryopump was added to the target region of the accelerator. The previously reported experiment was repeated, and no discoloration of the sample was observed. Figure 3.1.2 shows a damaged mirror with and without use of the cryopump. Note the discoloration observed in the case with poor vacuum.

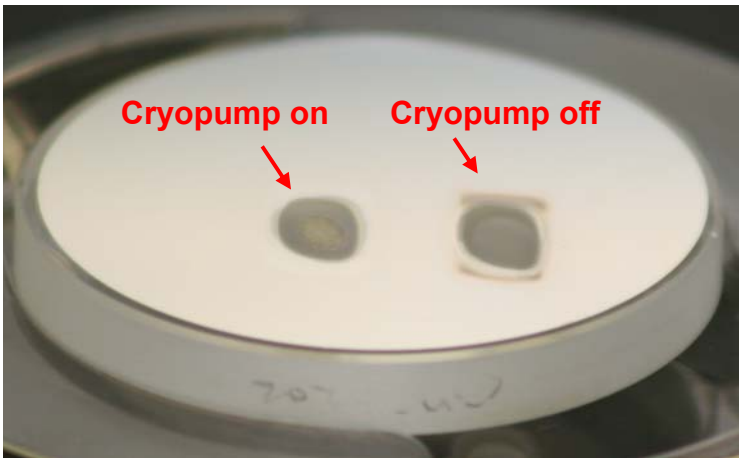

Fig. 3.1.2. A commercial mirror was irradiated with 3 MeV alphas with and without use of the cryopump to improve the vacuum conditions near the sample during irradiation.

Ion implantations were conducted at multiple angles to determine whether or not incidence angle was important. A single sample was irradiated at angles of 0 (normal), 60, and 78 degrees. The beam current was held constant, but the irradiation duration was extended for the grazing angles to provide the same total fluence (the irradiation was 2× as long at 60º as for 0º and 4.8× as long at 78º as for 0º). Prior to irradiation, the mirror surface roughness was 11.7 ± 1.8nm. The irradiation did not change the surface roughness at any of the angles. The "damage" only could be seen using the "breath method."

The final round of implantation experiments was performed at normal incidence using both 0.5 and 3.0MeV alphas. The lowest fluence used corresponded to approximately 3 days of exposure for a GIMM sitting 26 meters from target chamber center. Additional spots were exposed to 2-3 times this fluence. Figure 3.1.3 shows that the damage is nearly identical at the two ion energies. Additionally, the fluence is severe enough after the equivalent of ~9 days of operation in an IFE power plant that material actually flakes off of the mirror. Clearly this is unacceptable and bolsters previous arguments that local ion deflection is needed to protect the final optics.

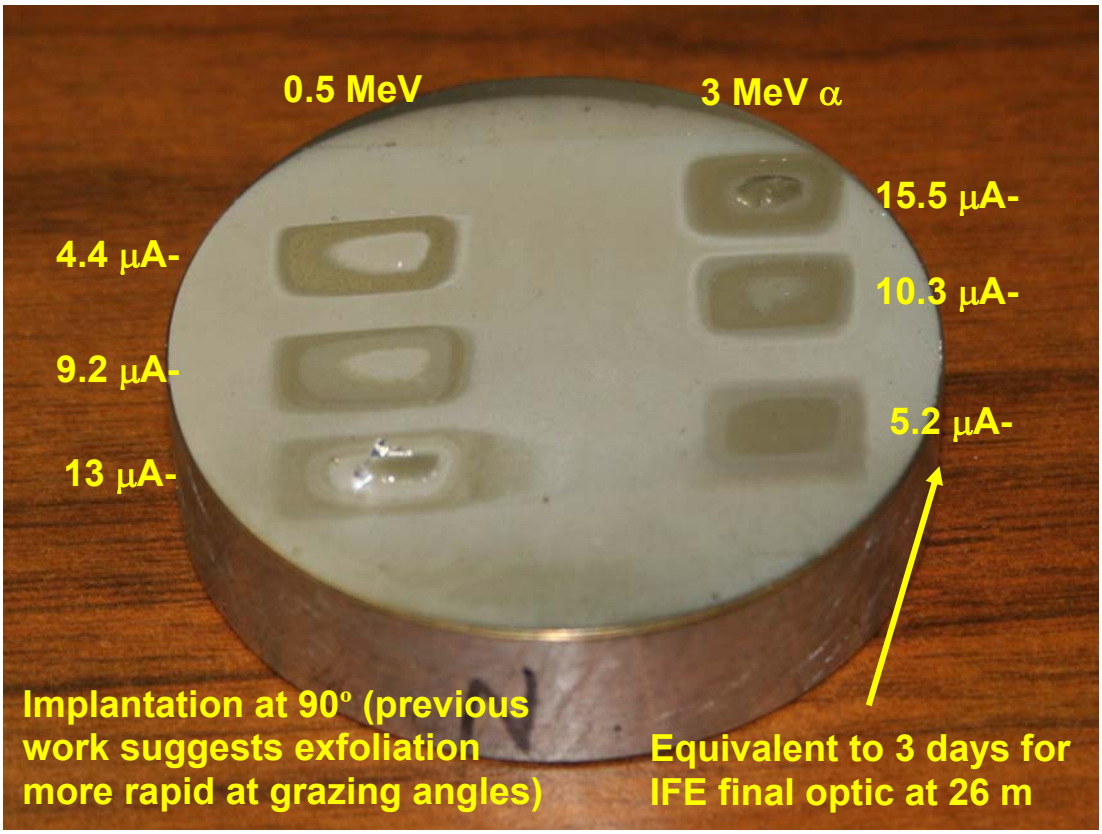

Fig. 3.1.3. An aluminum mirror shows catastrophic damage when irradiated with 0.5 or 3MeV alpha particles to fluences equivalent to ~1 week of operation in an IFE power plant.

Alpha implantation experiments for fused silica, which is the material proposed for use in the Fresnel lens final optic, showed relatively minor damage. Although a slight densification was observed, there was no exfoliation. However, RadHeat calculations show that a fused silica Fresnel lens would melt in a single shot if the ions are not deflected.

The above results were presented at the March and November 2005 HAPL meetings.

3.2 Ion Debris Mitigation Study

Our FY2005 tasks in the ion debris mitigation area were to:

- Continue modeling and design activities for a magnetic system to protect the final optics from burn and debris ion damage, and
- Provide self-consistent parametric results for a variety of ion deflection options.

In FY2005 we completed our preliminary analysis of the feasibility of using normally conducting electromagnetic coil pairs to deflect high-energy ionized debris that would otherwise threaten final optics in a laser-driven inertial fusion power plant. A basic depiction of the idea is shown in Figure 3.2.1. This work was summarized in detail in Ref. 1, and a journal article submission is being prepared.

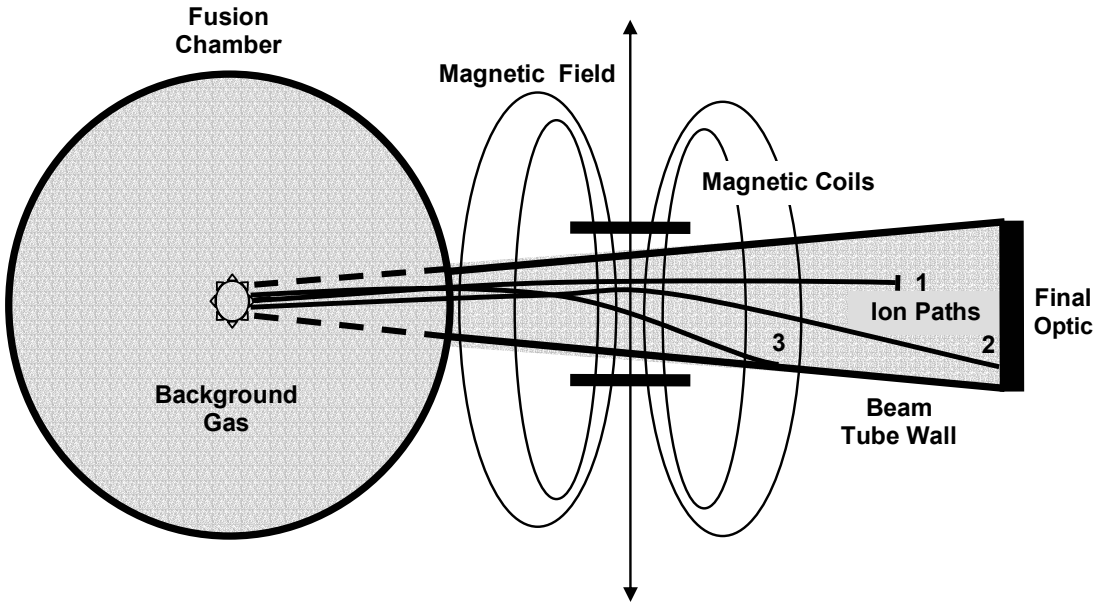

Figure 3.2.1. A depiction of the ion mitigation concept showing three possible ion paths: (1) stopping in the background gas, (2) an optic intercepting path, and (3) a path showing an ion successfully deflected into the beam tube wall.

The Deflector Code, described in last year's progress report, is used to model magnetic deflection of ion for optics protection. The credibility of the independent particle model used by Deflector when determining the interaction of the target ions with the coil generated magnetic fields was verified by performing ion transport simulations with LSP. This showed that the free streaming ion current at the magnetic coils is insufficient to produce plasma electric or magnetic fields capable of canceling the deflection forces resulting from the externally applied field.

Reference [1] includes sets of self-consistent ion deflection system parameters needed to protect the two final optic options (transmissive Fresnels or reflective GIMMs) for a range of potential driver types (KrF or DPSSL) and laser fluence limits. We concluded that normally conducting copper coil pairs from 1.0 to 1.8 m in diameter generating "center of coil pair" fields

of as little as 0.075 T could reduce charged particle fluence on final optics in all cases by factors greater than 10^4.

The power required for these magnets was estimated to be less than 6 MW in all cases. The cost of copper in the magnets and yearly operational costs were also estimated and found to be very modest at at $700k and $2.4M/year, respectively.

A systematic method for quantifying the threat from atoms sputtered off beam tube walls as a result of deflected ion impacts was refined, automated, and implemented. We analyzed sputtering from a smooth conical tungsten beam tube wall considering all the ion species emitted by the 350 MJ direct-drive HAPL target. We found that gold would produce significantly more sputtered atoms with the potential to reach the final optic than any other ion. However, it has not been determined if the calculated 2.9×10^{12} sputtered W atoms represent a significant threat or not.

References

[1] R. Abbott, "Ion Deflection for Final Optics in Laser Inertial Fusion Power Plants," UCRL-TH-217754 (Dec. 2005).

4.0 X-Ray Damage Studies

Our FY2005 tasks were to:

- Continue x-ray exposures and modeling for single crystal and powder metallurgical tungsten,
- Begin x-ray exposures for candidate final optic materials, and
- Generate x-ray damage and roughening data for multiple varieties of heated and unheated tungsten, including several x-ray fluences and numbers of pulses.

Considerable progress was made on XAPPER during FY2005. FY2004 XAPPER results were published in a special issue of the *Journal of Nuclear* Materials [1]. Early in FY2005, we realized that the source output appeared to be dependent upon the repetition rate. Unfortunately, our CCD camera, which is integral to x-ray fluence measurements, is unable to collect data at the desired frequency of 10 Hz. Faster cameras, shutters, and software tricks with the CCD were explored. Ultimately, two different options were implemented. First, we were able to take advantage of the CCD camera's readout time and use it to produce a series of spots within a single image. Figure 4.1 shows a series of nine spots collected in a single image with XAPPER pulsing at 10 Hz. By post-processing the images, we are able to separate out the individual spots and collect data at the full repetition rate of 10 Hz.

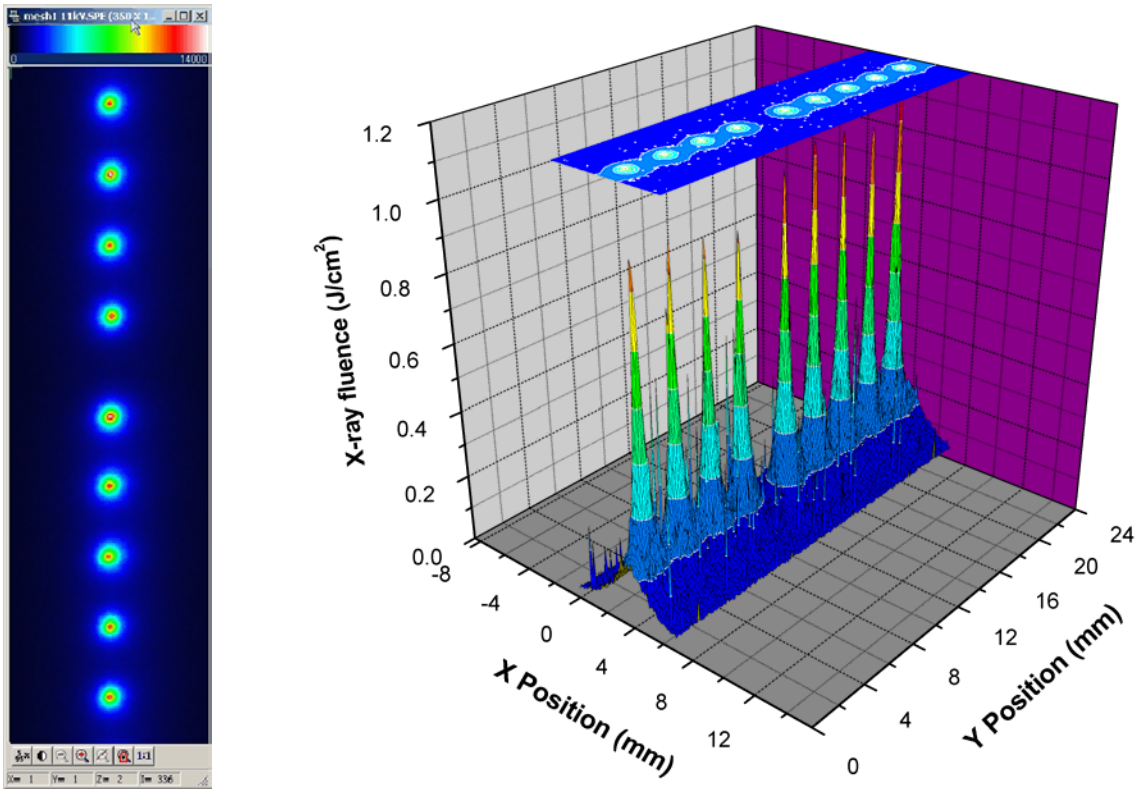

Fig. 4.1. Multiple x-ray spots can be captured in a single CCD image.

The first use of this new capability was to measure the x-ray fluence as a function of repetition rate and time. Figure 4.2 shows these results. Good stability is observed over time and the repetition rate effect is a mild one. Fluence is routinely measured at 10 Hz, which matches the operational conditions during exposure of most samples.

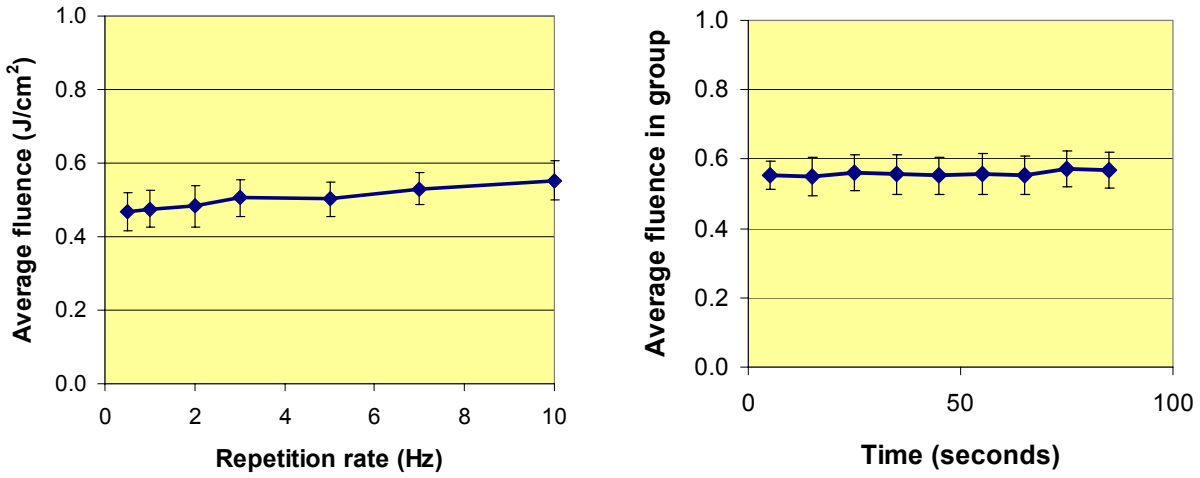

Fig. 4.2. X-ray fluence is mildly dependent upon repetition rate (left plot), but is quite stable over time (right plot).

The second method to measure fluence at 10 Hz was to implement a new CMOS camera that is capable of higher repetition rates than is our CCD camera. This effort was lead by Glenn Holland of the Naval Research Laboratory. After some difficulties with electromagnetic interference generated by XAPPER's plasma source, Mr. Holland succeeded in fielding the CMOS camera. The camera and first light image are shown in Figure 4.3. The "stars" in the image are repeatable and can be subtracted as background. The CMOS camera already has confirmed XAPPER's spot size and shot-to-shot stability of both focus and intensity. The CMOS is permanently fielded on the sample tray such that the chip sits (behind an x-ray filter) at the focal plane of the x-ray source.

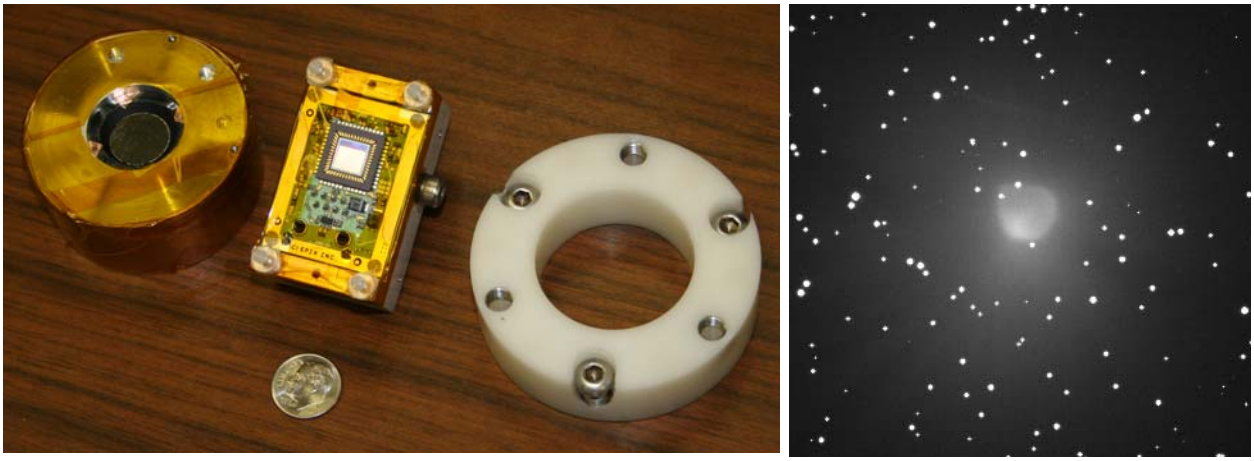

Fig. 4.3. The left image shows (from left to right) the x-ray filter assembly, CMOS camera, and vacuum feed-through / electrical isolation. The right image shows the first x-ray spot that was imaged with the CMOS.

The University of California at San Diego was subcontracted to build a non-contact optical thermometer for use on XAPPER. The instrument operates at 700 and 800 nm and uses

photomultiplier tubes with a subnanosecond risetime. The thermometer was installed early in FY2005, but we have been unable to get reliable signals to date. Various modifications are underway and will be reported on during FY2006.

A new sample heater was procured and installed during FY2005. It is capable of holding samples as high as 1200 °C during x-ray exposures. All samples exposed during this year were heated to 600 °C prior to the start of irradiation.

A powder metallurgical tungsten sample was exposed at ~0.7 J/cm^2 for 100, 1000, 10^4, 10^5 and 10^6 pulses. RadHeat calculations suggest that this x-ray fluence corresponds to a peak surface temperature of ~1800 ºC. Figure 4.4 shows scanning electron microscope (SEM) images of the location exposed to one million pulses. A series of concentric rings is observed: the innermost ring is roughly 50% the size of the x-ray beam spot size, while the faint, outermost ring is approximately the same size as the x-ray beam. Electron dispersive spectroscopy (EDS) shows that all structures, with the exception of the little white balls seen in the left image, are tungsten and tungsten oxides. The white balls are copper and presumably are erosion products from the x-ray source. The white balls are not seen inside the inner ring. We believe that they do, in fact, deposit near the center of the x-ray beam but that they are ablated away during subsequent x-ray pulses. Figure 4.5 shows a high-resolution SEM image of the outermost ring. We see what appear to be tungsten oxide "whiskers" coming out of the surface.

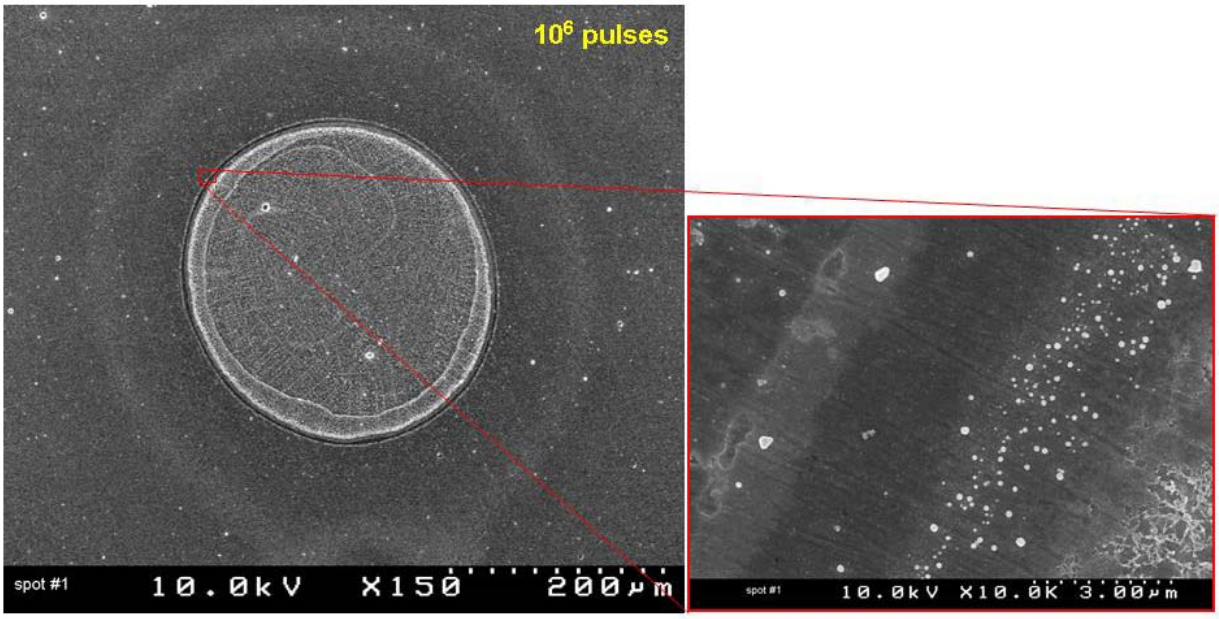

Fig. 4.4. SEM images of the 10^6 pulse damage spot show a pattern of concentric rings containing different structures of tungsten oxides.

Despite the visible damage, none of the spots appear to have experienced measurable surface roughening. Note that the delivered x-ray fluence should heat the surface only up to ~1800 ºC, while the goal is closer to 2500 ºC.

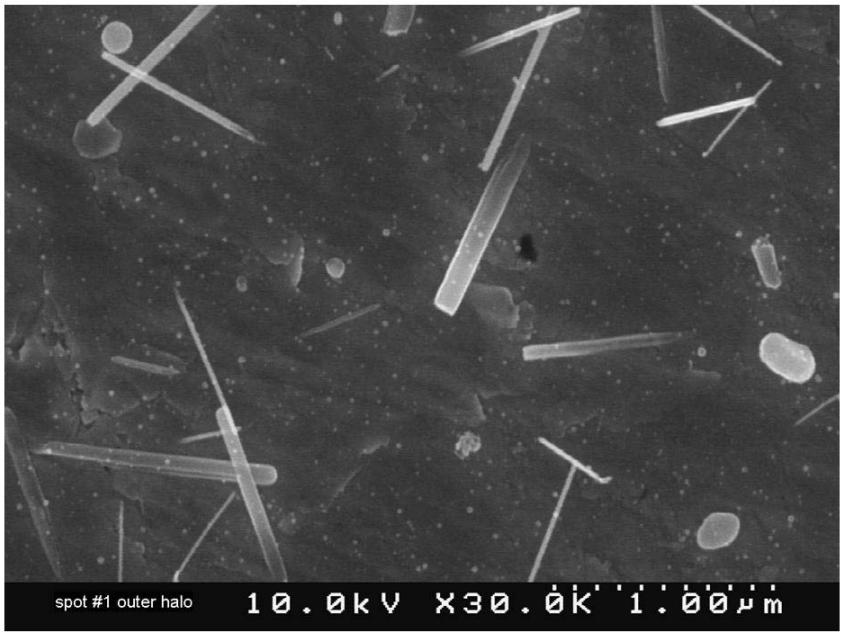

Fig. 4.5. Tungsten oxide whiskers appear to grow out of the surface. Dark regions of each whisker are in good electrical contact with the surface, while the bright spots are not.

A second powder metallurgical sample was exposed at the same fluence for 10^5 pulses in five separate locations in an attempt to observe repeatable results. Figure 4.6 is a photograph of the damaged region. Three of the five spots appear to be qualitatively the same, while two display considerably more damage. More puzzling is the fact that none of the spots display the concentric rings observed after 10^6 pulses at 0.7 J/cm^2.

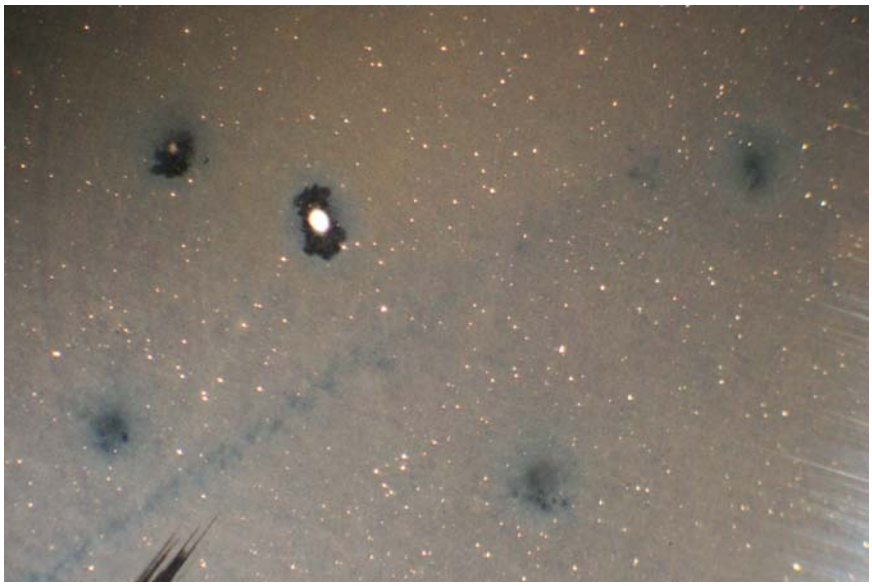

Fig. 4.6. Powder metallurgical tungsten was exposed in five spots to 10^5 pulses at ~0.7 J/cm^2.

One possible explanation lies in the fact that this is powder metallurgical tungsten. It might be the case that different grain orientations result in different manifestations of the damage. Alternately, the damage spots seen at 10^5 pulses, if hit with additional pulses, might

transform into something that looks more like what we see in the other sample with 10^6 pulses. The first theory could be tested with an experiment on a single crystal tungsten sample. If grain orientation is important, then all spots on a single crystal sample should look alike.

Fast photodiode experiments showed the XAPPER's x-ray pulse length is longer than originally believed. Accounting for the longer pulse length forced us to increase our target x-ray fluence from ~0.7 to ~1.0 J/cm^2 in order to reach the peak surface temperature goal of 2500°C. This higher fluence was used in subsequent experiments.

Next, two samples – one single crystal and the other powder metallurgical tungsten – were exposed. Each sample was hit in two different locations for 50,000 pulses at ~1 J/cm^2. Figure 4.7 shows these samples during irradiation of the second location. Note that the first damage spot can be seen on each sample (it is illuminated on each shot by scattered light).

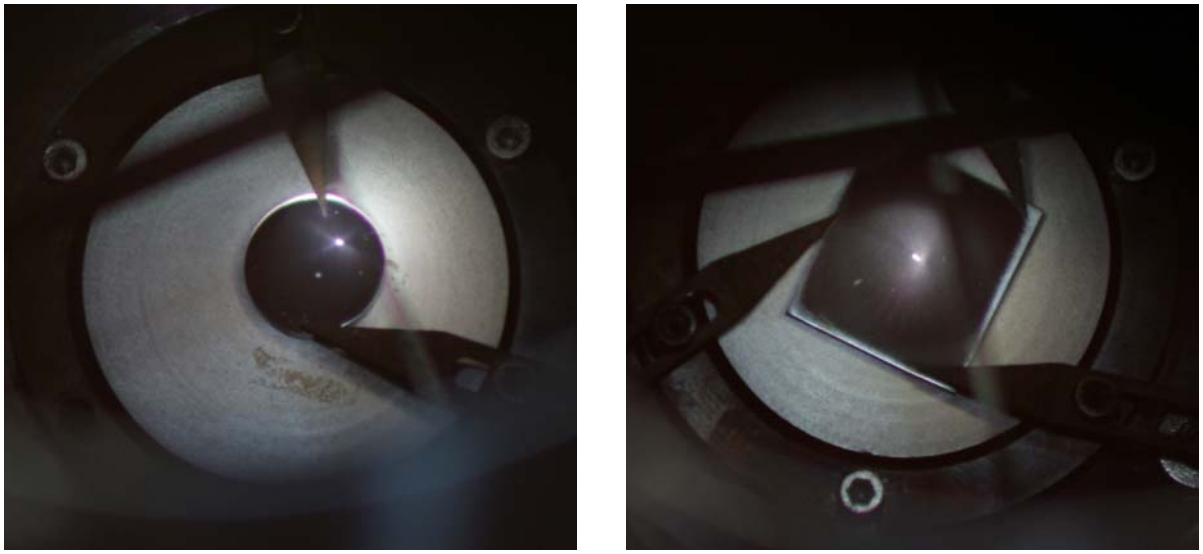

Fig. 4.7. Single crystal (left) and powder metallurgical (right) tungsten samples each were exposed in two different regions for 50,000 pulses at ~1 J/cm^2.

For the *powder metallurgical* samples, we see that both spots show considerable damage. The pre-irradiation surface roughness, as determined by white-light interferometry (WLI) was 24 nm R_a. After irradiation the first spot had a surface roughness of 170 nm, while the second one was 150 nm. While this agreement is encouraging, Figure 4.8 shows that the first damage spot has a region with significantly more roughening. We speculate that a particularly "hot" shot brought the material close to its melting point of ~3700 °C. Figure 4.9 shows a higher magnification view of this region in the first spot and a location near the center of the second spot.

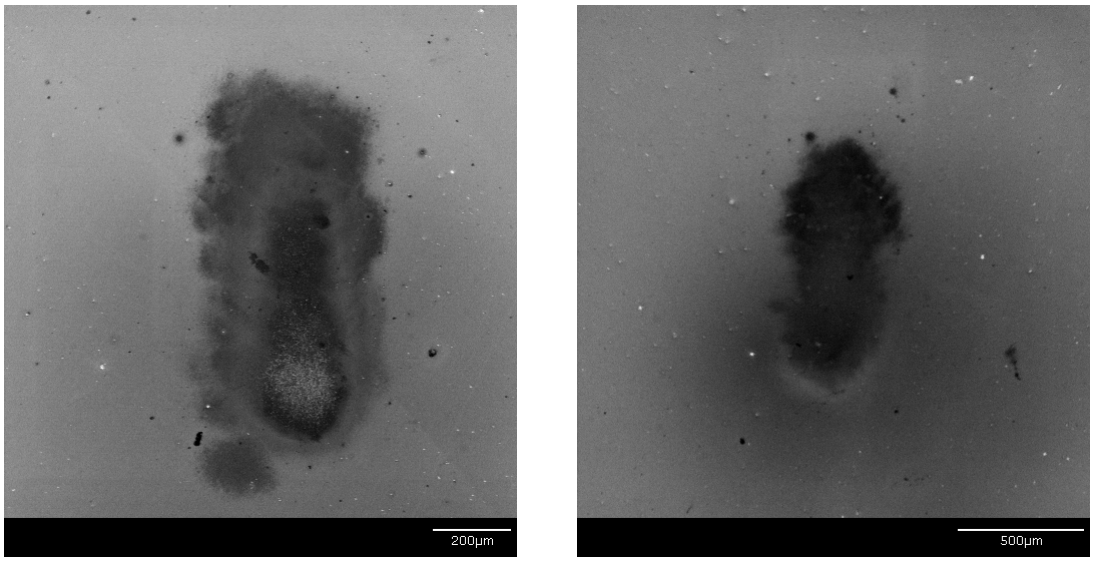

Fig. 4.8. The two damage spots on powder metallurgical tungsten look similar. The first spot (left) has a region near the bottom with significantly more roughening. Note that the scales are not equal.

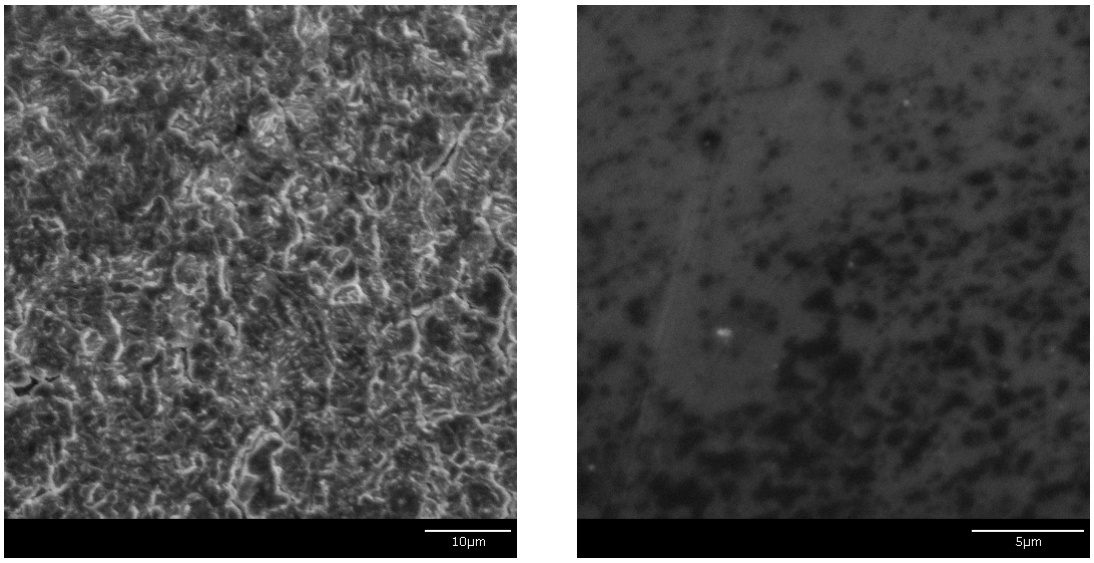

Fig. 4.9. A high-magnification view of the powder metallurgical tungsten shows significant roughening in one region of the first spot. Again, note that the scales differ between the spot #1 (left) and spot #2 (right) images.

Due to an error, the first spot on the *single crystal* sample received a fluence of only ~0.8 J/cm^2. This should have heated the surface to a peak temperature of ~2100 °C rather than the target temperature of 2500 °C that was achieved on the second spot. Despite this difference, the two single crystal spots look more similar than the two spots on the powder metallurgical sample that were exposed to the same fluence. This lends some credence to our theory of grain orientation being important, but it is too early to draw a conclusion. The pre-irradiation surface roughness was 14 nm. The first spot (T_{peak} ~ 2100 °C) roughened to 64 nm, and the second spot (T_{peak} ~ 2500 °C) roughened to 150 nm. Figure 4.10 shows high-magnification SEM images of

the center of each spot. A goal for FY2006 will be to repeat the single crystal irradiation for a larger number of spots (5-10) on a single sample.

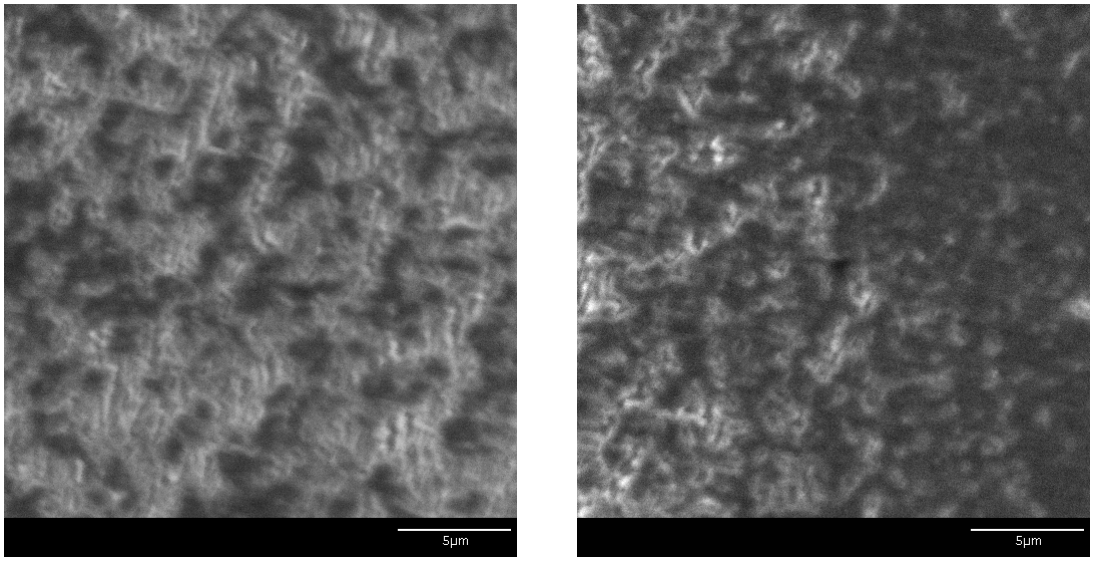

Fig. 4.10. SEM images of the center of each spot show that they are quite similar despite several hundred degrees differences in peak surface temperature.

We have begun evaluation of how laser optics should be irradiated on XAPPER. There are some key issues that must be addressed. If we assume that matching the peak surface temperature is again the goal, we will require very low x-ray fluences on XAPPER. Reducing the discharge voltage to several kV might provide a low enough fluence, but the shot-to-shot repeatability is inadequate. Another option is filtering of the x-ray beam, but this would be expensive and uncertain due to destruction of filters. Finally, we could design and fabricate a new mandrel that could be used to produce new ellipsoidal x-ray optics that focus differently than those currently in use on XAPPER. For example, an optic that intentionally brought the x-rays to focus in a larger spot could provide a lower fluence as well as the obvious benefits of the larger spot size.

Another issue for irradiation of grazing incidence metal mirrors is whether or not they actually need to be exposed at grazing angles. Doing so would be nearly impossible on XAPPER, and it is unclear that it is necessary. Evaluation of this and other issues will continue and experiments will begin in FY2006.

References

[1] J. F. Latkowski, R. P. Abbott, R. C. Schmitt, and B. K. Bell, "Effect of multi-shot x-ray exposures in IFE armor materials," *J. Nuc. Mater.* **347(3)** (Dec 2005) 255-265.

5.0 Target Design

The objectives in the area of target design were to complete analyses in five areas:

- Baseline target design,
- Target output threat spectrum,
- Dynamic zero-dimensional target model,
- Gain curves, and
- Laser-target specifications.

5.1 Baseline Target Design

Over the past two years, we have issued several prospective HAPL target designs with varying design and performance specifications. Accordingly, for standardization purposes, we have formulated a new standard baseline design for dissemination across the project. The new target radial build and materials are shown in Fig. 5.1.1.

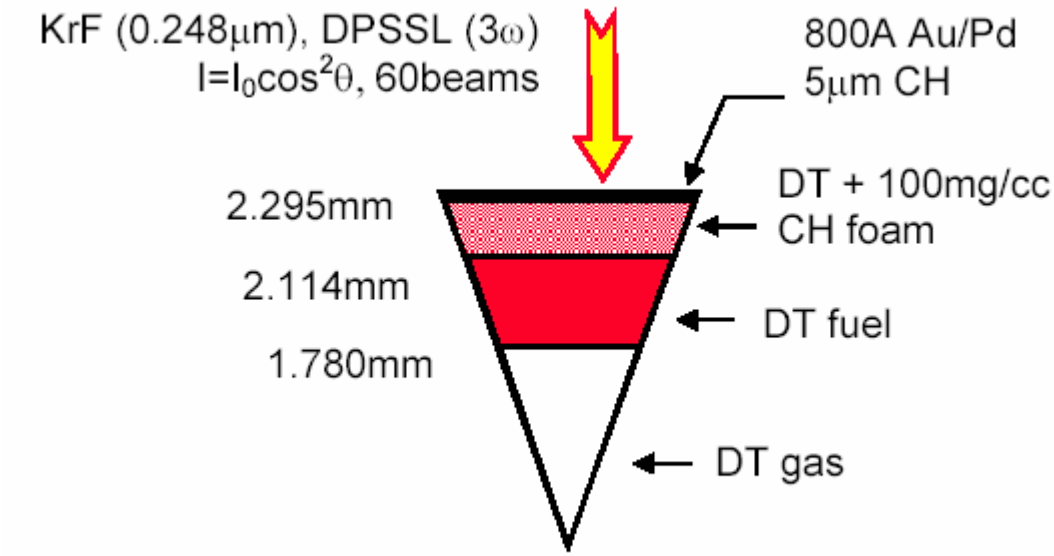

Fig. 5.1.1. New HAPL standard baseline target design.

The thin (800A) outer shell comprises a mixed 50:50 Ag/Pd gold overcoat for imprint reduction and IR reflection. This is vapor-deposited on a CH plastic shell, increased in thickness to 5 microns for adequate robustness. Prior to injection, the target temperature is maintained at 17.3 K. Accordingly, at compression time, the temperature of the gas plus DT fuel is taken to be ~17.3 K with the outer region of the target at ~18.5 K to account for target heating during injection.

The ablator is thinner than previous designs to minimize the fraction of unburned ablator left at ignition, thus minimizing high-energy CH/DT debris ions. This is at the expense of a larger rho-R at ignition and extra tamping. The (zoomed) gains can increase from ~150 to ~165

with thicker ablators that have ~30-40% left at ignition; however, the latter will be burdened with a higher energy content debris flux.

The laser drive pulse shape is shown in Fig 5.1.2 and is distinguished by a high intensity "picket" prepulse to set the ablator on a high adiabat, thereby enhancing its Rayleigh-Taylor stability through increased ablation velocity. The pulse shape is modeled as a prepulse plus four-shock system, i.e., picket, foot, 2nd shock, 3rd shock, and main shock. Pedestals were used for ease of locating shock convergence with rise/fall times of 100 ps (the assumed risetime capability of DPPSL and KrF). The rise/fall times can be increased to ~200-300 ps providing timing centroids and integrated energies are maintained; a slight timing retune would be required. Shocks 1-3 are timed to coalesce at inside edge of fuel at time of breakout of picket shock. The 4th (main) shock is timed to reach fuel/ablator interface at time when rarefaction shock from 1-4 coalescence reaches there.

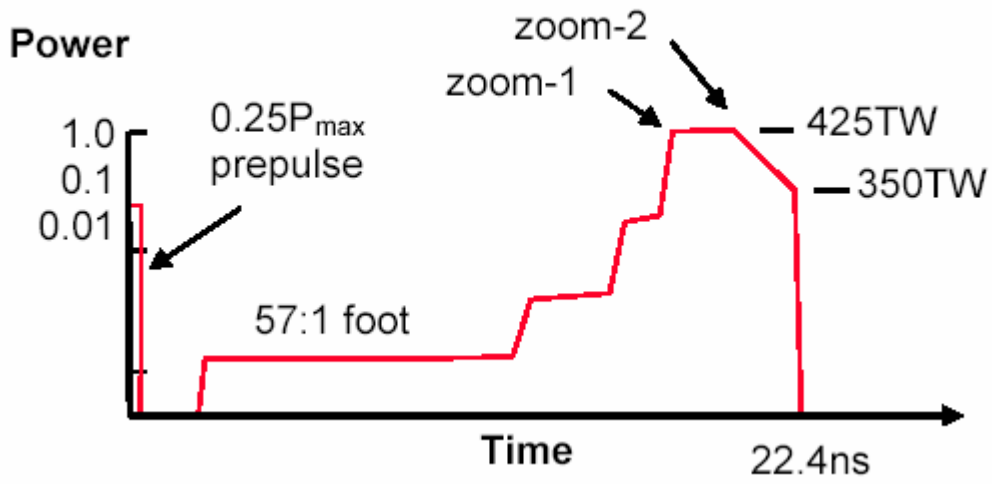

Fig. 5.1.2. Laser pulse shape for the baseline target.

Two zooms are used where spot size is reduced to critical radius at that time. The zoomed laser absorption fraction is ~98%, whereas the unzoomed absorption fraction would be ~90%

The new baseline target performance is shown in Table 5.1.3 under both KrF (0.248 μm) and DPSSL (0.349 μm at 3ω) illumination, and obtained from LASNEX, our standard radiation-hydrodynamic-burn code. Note from the pulse shape above that the peak power for KrF was reduced from a maximum of 425 TW at the second zoom point down to 350 TW in order to maintain the peak laser intensity at the critical surface consistent with a nominal LPI limit of $I\lambda^2 \sim 1.0\times10^{14}$ $Wcm^{-2}\mu m^2$ at λ=0.248 μm. The second and third columns show the DPSSL performance at the same peak power and same LPI limit, respectively.

Gains of ~150 at drive energies of ~2.5 MJ are obtainable with this target design. Without zooming, the gains would decrease to ~121 at a drive energy of ~3 MJ. Note that at the same peak power, the DPSSL-driven target is very similar to that of the KrF target. However, if we operate it at the same LPI $I\lambda^2$ limit, the gain decreases from ~150 to ~130.

Table 5.1.3. Performance Parameters for the New Baseline Target.

	KrF	DPSSL (3ω) at Same Peak Power	DPSSL (3ω) at Same Peak $I.\lambda^2$
Peak Power (TW)	350	350	180
Peak $I.\lambda^2$ ($Wcm^{-2}\mu m^2$)	~$1x10^{14}$	$1.9x10^{14}$	~$1x10^{14}$
E_laser (MJ)	2.46 (3.05 un-zoomed)	2.47	3.02
Yield (MJ)	365	367	383
Gain	148 (121 un-zoomed)	149	127
IFAR at 2/3r0	30.5		
Convergence ratio	33.4		
Peak shell velocity	$2.95x10^7$ cm/s		
Max rho-R at ign (g/cm2)	2.784		
KE margin at ign	0.39		

5.2. Target Output Threat Spectra

We have employed LASNEX to obtain target output (threat) spectra for the above target – that is, fusion burn products, x-rays and thermal debris – for use by other groups in chamber, optics and systems design studies.

Table 5.2.1 gives an energy accounting of the output spectra 100 ns after drive pulse initiation. At this time, the thermal content of the plasma is negligible (<<1%) and it can be assumed to be effectively free-streaming ballistic towards the chamber wall. The total energy output of 365 MJ of fusion yield plus 2.5 MJ absorbed laser energy is seen to be distributed between ~5 MJ (1.3%) of X-rays, 247 MJ (75%) of neutrons and 88 MJ (24%) of ions.

Table 5.2.1. Escape spectra at 100 ns after drive pulse initiation.

	Thermal Debris (J)	Burn and Nuclear Products (J)	Total (J)
X-rays	–	–	4.937×10^{6}
Gammas	–	1.680×10^{4}	1.680×10^{4}
Neutrons	–	2.743×10^{8}	2.743×10^{8}
Protons	6.255×10^{5}	1.137×10^{6}	1.763×10^{6}
Deuterons	1.166×10^{7}	1.006×10^{7}	2.1724×10^{7}
Tritons	1.733×10^{7}	9.166×10^{6}	2.650×10^{7}
^{3}He	3.171×10^{4}	4.607×10^{4}	7.777×10^{4}
^{4}He	3.556×10^{6}	2.673×10^{7}	3.028×10^{7}
^{12}C	6.879×10^{6}	8.834×10^{2}	6.880×10^{6}
^{13}C	8.366×10^{4}	1.141×10^{1}	8.367×10^{4}
Pd	1.844×10^{5}	<1	1.844×10^{5}
^{197}Au	3.607×10^{5}	<1	3.607×10^{5}
Pt	<1	<1	<1
	4.071×10^{7}	**3.214×10^{8}**	**3.671×10^{8}**
	(nuclear energy produced=3.647×10^{8} (=sum of thermonuclear energy plus exo- and endo-thermic in-flight reactions); laser energy absorb.=2.426×10^{6}; residual thermal energy=3.494×10^{4} J)		

A three-temperature black body fit to the X-ray escape spectra after 100 ns is:

$$E(T(\text{keV})) = \frac{c_1 T^3}{\text{Exp}[T/T_1]-1} + \frac{c_2 T^3}{\text{Exp}[T/T_2]-1} + \frac{c_3 T^3}{\text{Exp}[T/T_3]-1} \quad , \quad \text{J/keV}$$

where $c_1=1.24\times10^5$, $T_1=1.08$, $c_2=9.90\times10^2$, $T_2=4.30$, $c_3=4.85$, $T_3=1.51\times10^1$. The total integrated X-ray energy is 4.937×10^6 J and comprises ~1.3% of the total energy output

Fig. 5.2.2 shows a plot of the charged particle, neutron and gamma escape spectra after 100 ns where the charged particles are summation of thermal debris kinetic energy plus burn and nuclear products. Because there is negligible burn product interaction, the spectra for the high-z Pd and Au ions are just KE debris spectra.

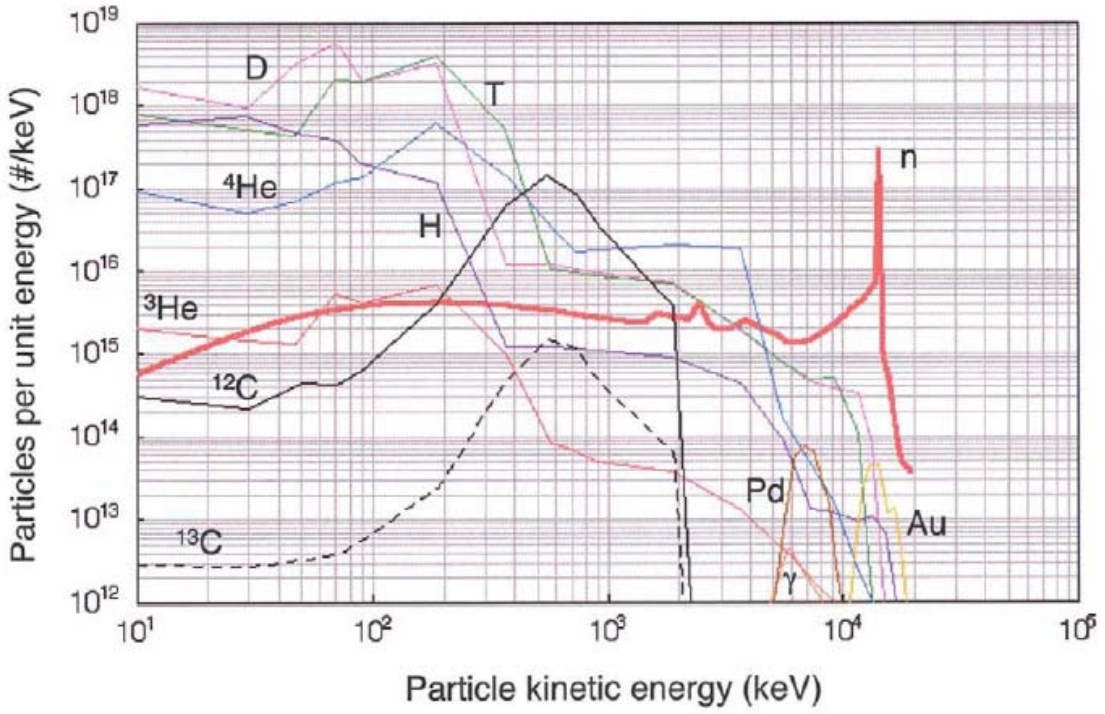

Fig. 5.2.2. Charged particle, nuclear and gamma escape spectra.

5.3. A Dynamic Zero-Dimensional Model for Compression, Ignition and Burn

In the field of target design, there are a number of design parameters that must be determined to optimize a given configuration for a particular mission. Given that, even in 1-D, typical rad-hydro calculations take minutes per design point through ignition and burn, a prohibitive amount of computational time would be expended to formally map design space. A number of simple zero-dimensional models to aid target scoping have been formulated over the past two decades based on time-independent isobaric assumptions. However, our observations of full 1-D simulations of the direct-drive target designs for HAPL show that this common wisdom of isobaric (constant pressure) conditions around stagnation/ignition is incorrect. In particular, we conclude that hotspot formation, ignition and burn are dynamic processes such that even zero-dimensional models must be time-dependent to provide an adequate description of the physics.

Consequently, we have completed a fully dynamic 0-D model based on six coupled ordinary differential equations that describe energy, momentum and mass balances across the hotspot/cold fuel system. This year, the model has been converted and extended to run under *Mathematica-V* with its improved ODE solver. Good agreement with 1-D simulations is obtained for integral performance quantities with run times of only ~1-2 seconds per case.

5.4 Gain Curves for Inertial Fusion Targets

The target gain curve (i.e., fusion energy gain as a function of driver energy) for an inertial fusion target of a given class is a central consideration for the power plant design. However, the formal process of obtaining such data self-consistently is a complex undertaking. In particular, as the driver energy changes, the target characteristics must change to optimize performance subject to constraints such as ignitability and stability. Accordingly, every point on a gain curve is a different optimized target design.

Fig. 5.4.1 shows the gain curve for the single fixed target design described above. Note that as the laser drive energy is reduced from high values, the target gain actually increases up to a maximum value. This is because the target is being over-driven at high energies and ignites before fully assembling. As the drive energy is reduced, ignition is increasingly delayed, allowing the in-flight fuel shell to stagnate at higher areal densities. Finally, however, the shell has insufficient kinetic energy to create the hotspot and an ignition cliff is seen around an energy of ~2 MJ. Note that adjustment of the laser drive energy would enable gain and yield control for each injected target.

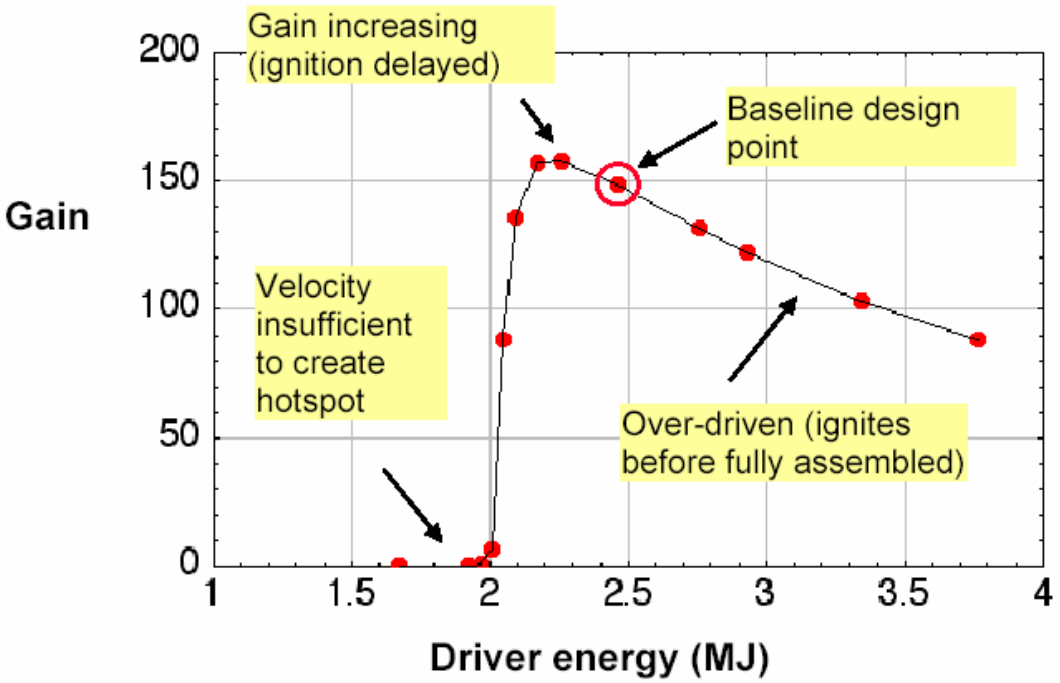

Fig 5.4.1. Gain curve for the fixed HAPL baseline target.

We have obtained an initial set of nominal (conventional) gain curves for this class of direct-drive target by using scalings obtained last year and renormalizing to the new target performance parameters in Table 5.1.3 above. These are shown in Fig. 5.4.2. Note also that

under these scalings, a 1 MJ-class direct-drive target would exhibit a gain of ~50 at 3ω. Thus, this is quite consistent with present NIF direct-drive target designs being conducted by LLE (University of Rochester) at the same energy.

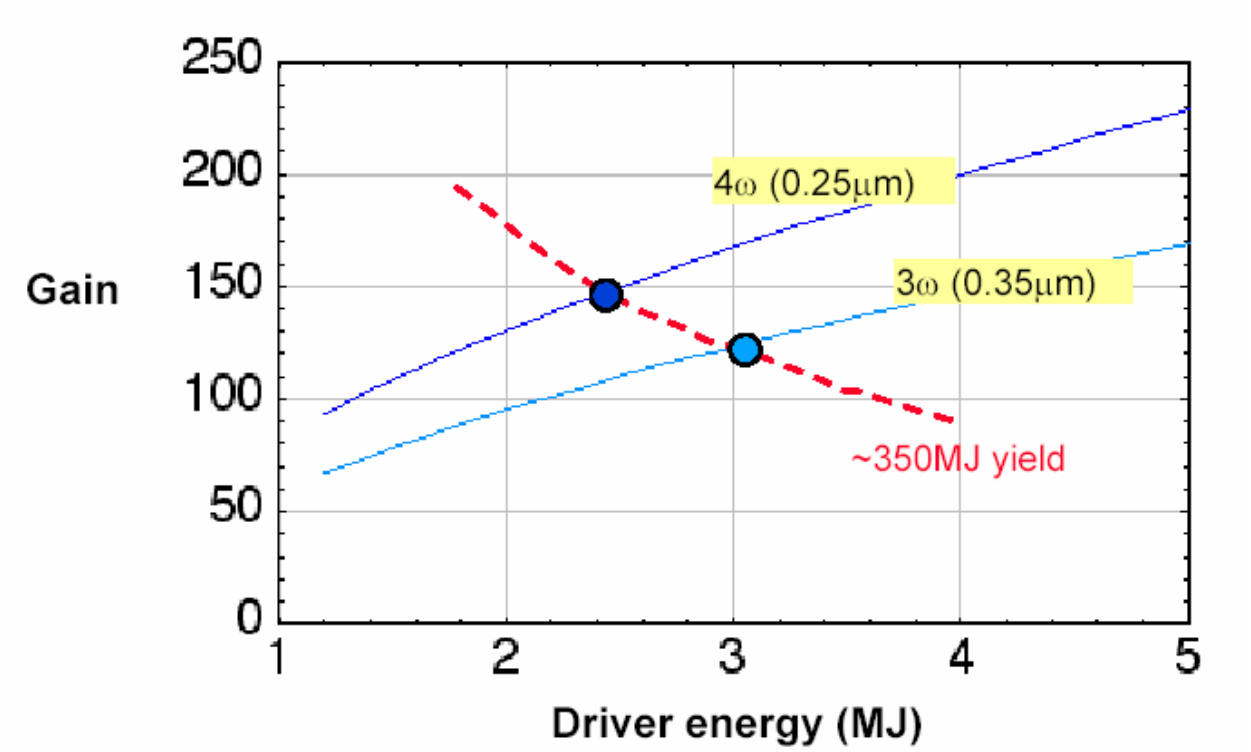

Fig 5.4.2. Nominal gain curves for KrF and DPSSL (3ω) driven direct-drive targets. The curves can be fit to laser drive energy E(MJ) with a function of the form: Gain ~ a $(E-b)^{0.585}$, where for KrF: a=90.6, b=0.138; for DPSSL at 3ω: a=67.8, b=0.210

We are now formulating methodologies for determining gain curves with self-consistent constraints. Our preliminary ideas are represented in Fig 5.4.3. We suggest that, formally, there are seven independent variables that must be defined to delineate a target design, namely: driver energy on target, laser wavelength (blue, green, etc), laser power over the peak portion of the drive, shell outer radius, ablator thickness, fuel thickness and the in-flight adiabat. Future work on the 0-D *Mathematica* code will attempt to delineate this design space.

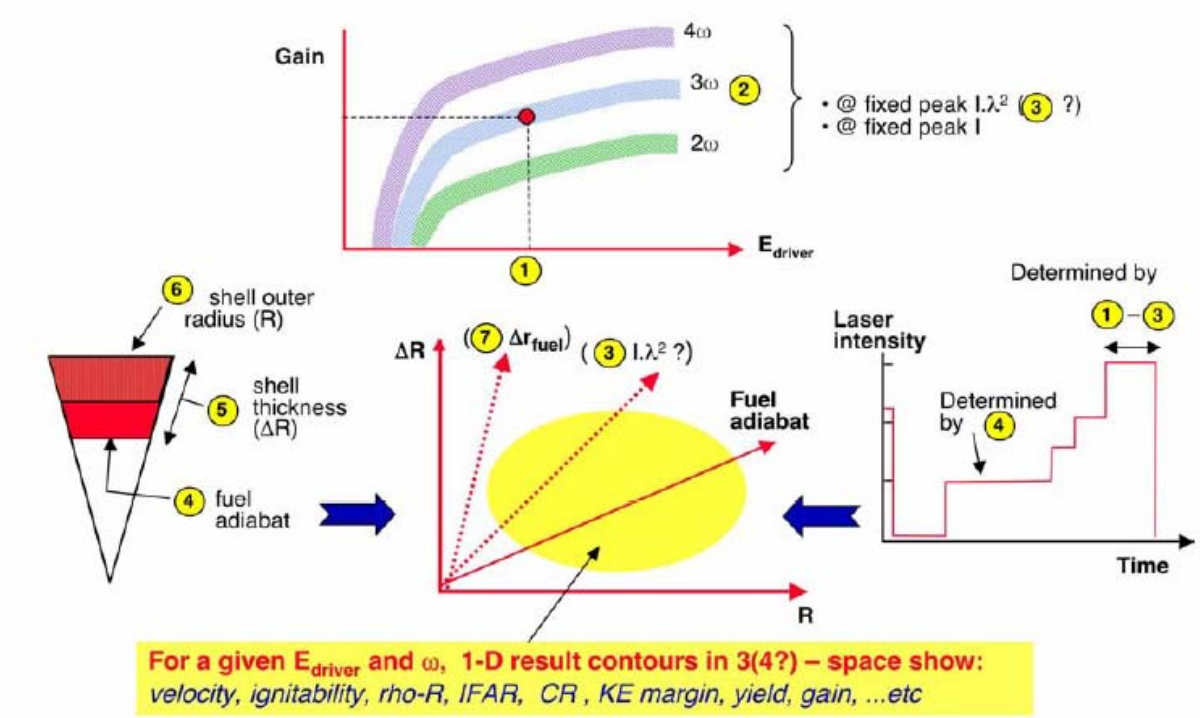

Fig 5.4.3. Mapping of direct-drive target gain space requires seven independent parameters

5.5 Laser-Target Specifications

Based on the new baseline target design above, we have formulated a draft set of design specifications for the HAPL laser/target system. These are shown in Table 5.5.1.

Table 5.5.1. HAPL Laser-Target Design Specifications.

Energy on target, typical (MJ)	~2.5-3.5 MJ dependent on wavelength (2-4ω)
Pulse lengths, typical (ns)	Total ~25, time at peak power ~5 (see target specific pulse shape specs)
Power, typical (W)	$<5x10^{14}$(peak), $\sim 1x10^{14}$(picket), Contrast ratio<=60 (see target shape specs)
Intensity, typical (W/cm^2)	$\sim 1x10^{15}$ (over av. peak power) (see target specific specs)
Pulse shape shock precision: time/power	± 0.05ns (± 0.3ns -> -7% in gain); ± 3% (± 10% ->-7% in gain)
No of ports	60**
Beam intensity profile and focus	Quadratic (=cosine-squared); focus at target diameter at t=0 (see specific target specs for zooming)**
Beam-beam power bal	8% in 0.5ns
Quad-quad power bal	4% in 0.5ns (indep quads)
Individual beam non-uniformity	3% in 0.5ns (all modes)
Bandwidth/smoothing/RMS imprint	1THz (3ω) / 2D SSD / 50nm
Polarization smoothing	2x50 μrad (needed?)
Overall uniformity; low modes (beam-beam variation; pointing, power-bal.....)	dl/l=1.5% (for CR=30,del-$r_h/r_h \leq 1/3$)
Overall uniformity; high modes l=10-120 (from individual beam structures)	<0.5% RMS for t_{smooth}=0.5ns (indiv beam uniform. ~3%)
Laser alignment /target tracking	± 20 μm rel to target center
Capsule outer CH surface finish	<50 nm *
Inner ice layer uniformity/ roughness	± 5 μm (± 20μm -> -7% in gain); <0.5μm for $l \geq 10$ (NIF direct drive specs as a placeholder)*

Sources:

J. Perkins HAPL workshop presentations UCLA (June 2004), PPPL (Oct 2004)
D. Eimerl "Configuring NIF for Direct Drive" UCRL-ID-120758 LLNL (1995)
R. McCrory "NIF Direct-Drive Ignition Plan" plus briefing VGs (April 1999)
LLE Reviews **98** p67, **79** p121, **84** 181
S.Skupsky (LLE) pvt comm. (May 2005)
* NIF indirect drive specs: 12 nm (CH), 33 nm (Be/Cu), 0.5 μm (inner ice l >10)
** Placeholder specs. See also "Port Placement and Illumination Uniformity", Malcolm McGeoch, HAPL meeting, June 20th 2005, Livermore, CA

FY 2006 STATEMENT OF WORK

1.0 DPSSL Development

Task 1.1 Fabricate High Quality Yb:S-FAP Crystals
Continue fabrication and growth of gain media for Mercury laser both at LLNL and commercial facilities. Focus will be on improving crystal quality and size. Produce coated and characterized slabs for the laser system.

Task 1.2 Full Mercury Laser System Activation
Fully activate system with two gas cooled amplifiers for average power operation >600 W at 1.047 μm. Diagnose performance with a suite of diagnostic packages to measure spatial, temporal, wavefront and energy characteristics. Benchmark codes with data. Demonstrate frequency conversion and perform integrated tests at 2ω on the Mercury Laser – with 50% conversion at a repetition rate > 5 Hz. Perform first light demonstration of third harmonic generation (3ω).

Task 1.3 Advanced Technologies
Complete offline demonstration of advanced front end laser and active wavefront correction technology and begin installation on the Mercury laser system. The main system controls and diagnostics will be upgraded to accommodate these new systems. Investigate advanced component technologies for improving laser performance including: spatial filters, high damage threshold optics, average power isolation components, and high power diode bars. Continue to develop integrated fusion driver concepts.

2.0 Chambers

Task 2.1 Chamber Response & Safety and Environment
Continue to apply the RadHeat code to IFE chamber and final optic issues, including the magnetically-protected chamber concept. Complete a safety and environmental assessment for the candidate blanket designs. Define and scope key experiments for chamber/laser interface issues related to fast ignition approach to IFE.

Task 2.2 Systems Modeling and Design Integration
Continue development of scaling relationships for fusion chambers, blankets and power conversion systems. Incorporate new KrF and DPSSL models (developed by laser designers) into the laser IFE systems code. Assist in the development of an integrated design concept. Assess power plant design configurations and interface issues to take advantage of fast ignition approach to IFE.

3.0 Final Optics

Task 3.1 Irradiation Studies
Anneal, polish and complete laser damage testing of neutron-irradiated fused silica samples. Produce fused silica Fresnel lens (4-6" aperture) using lithographic fabrication techniques. Select possible constituent materials (fused silica, calcium fluoride, etc.) for use in the dielectric focusing optic. Survey/measure relevant parameters such as optical absorption, refractive index, and coefficient of thermal expansion. Procure samples of the most promising materials and coordinate with ORNL personnel to have neutron irradiations completed.

Task 3.2 Ion Debris Mitigation Study
Identify uncertainties in the base case magnetic protection system for the final optics. Define and scope key scaled experiments to address those uncertainties. Complete coupled ion deflection calculations to address thermal issues for the ion beam dumps.

4.0 X-ray Damage Studies

Task 4.1 X-ray Damage Studies
Continue x-ray exposures and modeling for both chamber armor (tungsten) and final optic (aluminum and fused silica) materials. Generate x-ray damage and roughening data for the final optic materials at several x-ray fluences and numbers of pulses.

5.0 Target Design

Task 5.1 Target Performance Parameters and Output Threat Spectra
Produce baseline target design(s) for dissemination across the project. Calculate target performance parameters (gain, yields, etc) and target output threat spectra (burn products, x-rays, thermal debris). Assess 2D stability with full beam geometry.

Task 5.2 Dynamic 0-D Models for Compression, Ignition and Burn
Extend the development of the non-isobaric dynamic target model with application to (a) scoping direct drive target design and optimization issues (b) obtaining sets of frequency-dependent direct-drive gain curves.

Task 5.3 Advanced Target Designs
Commence scoping studies for advanced HAPL target designs with the object of obtaining higher gains, lower drive energies and facilitating non-4π (non-spherically symmetric) drive. Candidates include: (a) two-sided asymmetric direct-drive and (b) shock fast-ignited direct drive.

6.0 Integrated Technology Demonstration

The Mercury laser will be configured to support final optic and first wall studies, material lifetime characterization and laser-plasma interaction experiments relevant to the NNSA programs and fusion sciences

FY 2006 COST BY ELEMENT (Total = $9,800,000)

1.0	DPSSL		
	1.1	Fabricate Yb:S-FAP Crystals	$2,082,000
	1.2	Full System Activation with Two Yb:S-FAP Amplifiers	$3,572,000
	1.3	Advanced Technologies	$2,113,000
2.0	Chambers		
	2.1	Chamber Response & Safety and Environment	$90,000
	2.2	Systems Modeling and Design Integration	$80,000
3.0	Final Optic		
	3.1	Irradiation Studies	$240,000
	3.2	Ion Debris Mitigation Study	$40,000
4.0	X-ray Damage Studies		$353,000
5.0	Target Design		$250,000
6.0	Integrated Technology Demonstration		$980,000

TECHNICAL CONTRIBUTORS TO THIS PLAN

Lawrence Livermore National Laboratory

Ryan Abbott (Chambers, Final Optics, X-ray Damage)
Paul Armstrong (Front End Laser)
Andy Bayramian (Laboratory experiments)
Ray Beach (IRE)
Chris Ebbers (Frequency Conversion, Editor)
Alison Kubota (Molecular Dynamic Simulations)
Jeff Latkowski (Chambers, Final Optics, X-ray Damage)
Zhi Liao (Wavefront Control)
Wayne Meier (Chambers, Systems Modeling)
Joe Menapace (MRF Phase Plate Technology)
Bill Molander (Mercury Laser Raytrace simulations)
John Perkins (Target Design)
Susana Reyes (Safety and Environment)
Kathleen Schaffers (Crystal Growth)
Steve Telford (Control System)

LLNL Managers:
Ed Moses (Associate Director for the National Ignition Facility Programs)
Camille Bibeau (Program Manager)
Wayne Meier (Deputy Program Leader for IFE)